

Article

Fractional Crystallization and Partial Melting of the Paleoproterozoic Gneisses and Pegmatite in the Giant Husab Uranium Deposit, Namibia

Shan-Shan Li ¹, Wei Zeng ², Huai-Feng Zhang ³, Lu Wang ¹, Espine Tuyakula Shivute ¹ and Kun-Feng Qiu ^{1,*} 

¹ State Key Laboratory of Geological Processes and Mineral Resources, School of Earth Sciences and Resources, China University of Geosciences, Beijing 100083, China; lishanshan199811@163.com (S.-S.L.); 2001210050@email.cugb.edu.cn (L.W.); 9101190003@cugb.edu.cn (E.T.S.)

² Tianjin Center, China Geological Survey, Tianjin 300170, China; zwei2011@mail.cgs.gov.cn

³ Uranium Resources Company Limited, China General Nuclear Power Corporation, Beijing 100029, China; njdxzhang@163.com

* Correspondence: kунfengqiu@cugb.edu.cn



Citation: Li, S.-S.; Zeng, W.; Zhang, H.-F.; Wang, L.; Shivute, E.T.; Qiu, K.-F. Fractional Crystallization and Partial Melting of the Paleoproterozoic Gneisses and Pegmatite in the Giant Husab Uranium Deposit, Namibia. *Minerals* **2022**, *12*, 379. <https://doi.org/10.3390/min12030379>

Academic Editor: Harald G. Dill

Received: 11 February 2022

Accepted: 18 March 2022

Published: 19 March 2022

Publisher's Note: MDPI stays neutral with regard to jurisdictional claims in published maps and institutional affiliations.



Copyright: © 2022 by the authors. Licensee MDPI, Basel, Switzerland. This article is an open access article distributed under the terms and conditions of the Creative Commons Attribution (CC BY) license (<https://creativecommons.org/licenses/by/4.0/>).

Abstract: The giant Husab uranium deposit is located in the Paleoproterozoic Abbabis Metamorphic Complex, which was highly partially melted and metamorphosed during the Damara Orogenic Event. The timing of Magma emplacement has been investigated; however, the petrogenesis is unclear. Here we reported petrology, geochemistry, and monazite U-Pb age data from biotite granitic gneisses, syeno-granite, syeno-granitic pegmatites, syeno-granitic gneiss, granitic syenite and biotite quartz monzonites of this complex. Geochemical data suggest that these Paleoproterozoic rocks show high SiO₂, Al₂O₃, and K₂O, moderate Na₂O, low CaO and Fe₂O₃, and MgO abundance. The alkali-calcic to alkalic, peraluminous, low Fe-number, depletion in HFSE (Nb-Ta, Ti) and enrichment in LILE (e.g., Rb, Pb) characteristic correspond with I- and S-type granite. Major and trace elements are strongly fractionated with the increase of SiO₂, which, together with strongly fractionated LREE patterns and high (La/Yb)_N ratios of the biotite granitic gneiss and syeno-granitic gneiss, suggest that the Magma was highly evolved and fractionated. Monazite U-Pb data show three metamorphic age groups of 581–535 Ma, 531–522 Ma and 518–484 Ma. The increasing trend of La/Sm and La/Yb with the increase of La, suggest these rocks most likely experienced a partial melting process during the late Palaeozoic metamorphism. We, thus, propose a fractional crystallization model for the generation of the Paleoproterozoic Abbabis Metamorphic Complex basement rock, which was metamorphosed and melted during the late Palaeozoic Damara Orogenic Event and provided the Magma sources for primary uranium mineralization.

Keywords: monazite U-Pb geochronology; fractional crystallization; partial melting; Abbabis Metamorphic Complex; Husab uranium deposit

1. Introduction

The Damara Orogenic Belt (DOB) comprises Paleoproterozoic (ca. 2026–1750 Ma) basement gneiss and amphibolites, covered by the passive Margin Neoproterozoic (ca. 780–600 Ma) sedimentary sequences of the late Proterozoic Nosib (ca. 750 Ma) and Swakop groups, and intruded by Neoproterozoic and Paleozoic (ca. 660–550 Ma) granitoid-diorites [1–5]. The basement gneiss is strongly migmatized and underwent anatexis [6] and metamorphism during the Damara Orogenic Event (ca. 580–510 Ma) [3,7]. The Neoproterozoic and Paleozoic granitoid-diorite intrusions are considered to form by the products of partial melting of the basement gneiss [4,8–12]. Among those younger intrusions, the highly evolved granitic intrusions are generally formed associated with uranium deposits during the late Proterozoic, such as the Rössing and the Husab mines [13–18]. The late Proterozoic uraniferous leucogranite show negative ε_{Nd} values and late Neoarchean to

Paleoproterozoic Nd model ages of 2.0–2.5 Ga, suggesting that the Magmatic source for the primary uranium mineralization is derived from the Paleoproterozoic basement [8,9]. Thus, investigation of the basement rocks provided important evidence to trace the sources of uranium and the metamorphic history of the Damara Orogenic Event.

The Paleoproterozoic Epupa and Hohewarte metamorphic complexes are well studied and generally correlated with the Abbabis Metamorphic Complex (AMC) [3,4,6]. In the Epupa Metamorphic Complex, the granitoid gneisses are calc-alkaline, and metaluminous to peraluminous, which, together with the lithological association of amphibolite and gabbros, a Magmatic arc setting is proposed [4,6,19,20]. The Hohewarte Metamorphic Complex is comprised of granitoid gneisses, amphibolite, anorthosite, metanorite, metagabbro, and serpentinite. These granitoid gneisses are calcic to alkalic, peralkaline to peraluminous, and exhibit low light rare earth element (LREE) and high heavy rare earth element (HREE) abundance, which represent a metasomatised Mantle source generated in a subduction setting [3].

Previous studies reported zircon U-Pb ages and show the Abbabis Metamorphic Complex formed at ca. 2093–2014 Ma [21], and partial melting of these gneisses generated the early Paleozoic (ca. 547–497 Ma) Magmatic intrusions and the primary uranium mineralization [8,14,15], whereas their petrogenesis remains ambiguous. In this study, we present the results from coupled petrology, whole-rock geochemistry, and monazite U-Pb geochronology to constrain the petrogenesis of the Abbabis Complex, and the correlation of metamorphism with the intrusive granite formation during the Damara Orogeny.

2. Geological Background

The Neoproterozoic DOB forms one of the Pan-African Orogenic Belts, which intersects to the west with the Kaoko Belt and to the east with the Zambezi Belt [22,23]. The Damara Orogenic Belt extends ENE–WSW, which welded the Congo Craton in the northwest and Kalahari Craton in the southeast by the ocean closure of Kalahari Sea during ca. 580–520 Ma [2,24–30]. Based on the structure, stratigraphy, geochronology, and metamorphic grade, the DOB can be divided into a Northern Zone (NZ) and Northern Platform (NP), Central Zone (CZ), Southern Zone (SZ) and the Southern Margin Zone (SMZ) [2,24,31] (Figure 1A).

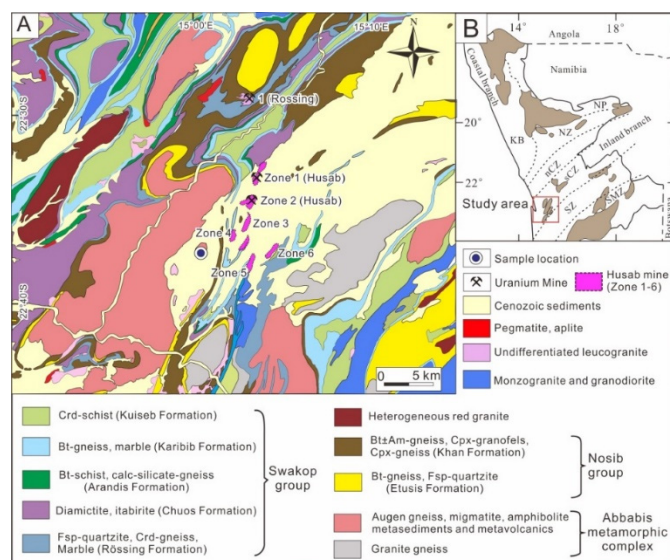


Figure 1. (A) Regional Map showing distribution of various domes, the Abbabis Metamorphic Complex spatially associated with primary uranium deposits of the Central Zone. (B) Geological framework of the Damara orogen showing the study area within the Central Zone, Namibia. Abbreviations in inset: KB: Kaoko Belt, NP: Northern Platform, NZ: Northern Zone, nCZ: Northern Central Zone, sCZ: Southern Central Zone, SZ: Southern Zone, SMZ: Southern Marginal Zone [2,8,14].

The Central Zone is subdivided into north (nCZ) and south (sCZ) Central Zones by the Omaruru Lineament, and experienced amphibolite facies metamorphism with lower granulite facies metamorphism in the western part [32,33]. The nCZ is composed of turbiditic graywackes, Marble, conglomerates, and pelitic schists alternating with calc-silicate bands, which belong to the Kuiseb and Karibib Formations [2]. The sCZ comprises of Paleoproterozoic (ca. 2.0–1.8 Ga) basement gneiss and amphibolites, and the Neoproterozoic (ca. 750–600 Ma) sedimentary sequence of the Damara Supergroup, intruded by syn- to late- and post-tectonic granite and minor diorites, tonalites, and granodiorites during ca. 570–480 Ma [34–36].

The Abbabis Metamorphic Complex in the sCZ of the Damara Orogenic Belt is considered as the pre-Damara basement, which comprise of Paleo-Mesoproterozoic (ca. 1925 Ma, ca. 1300–1100 Ma) quartzofeldspathic gneiss, augen gneiss, banded gneiss, amphibolite dykes, and supracrustal rocks, and experienced the Pan-African orogenic metamorphism and partial melting [21,33] (Figure 1B). The AMC is covered by the Neoproterozoic metasedimentary rocks of the Nosib and Swakop Groups. The sedimentary rocks of the Nosib and Swakop Groups comprise of quartzite, arkoses and conglomerate, calc-silicate rocks, Marble, metapelitic schist, and glaciogenic diamictites [2]. The Nosib Group comprises of the Etusis and the Khan formations. From bottom to top, the Swakop Group consists of the Rössing, Chuos, Karibib, and Kuiseb Formations. The basement and sedimentary sequence are intruded by extensive early Paleozoic granite comprising 96% of the succession with minor diorite, granodiorite and Mafic rock comprising 4%. The giant Husab uranium deposit is formed within the Rössing and Khan Formations during the late Paleozoic Magmatic event [17,18].

The studied samples are collected from a large quarry of the Abbabis Metamorphic Complex, which is located in the southwest of the Husab uranium deposit ($15^{\circ}00'27''$ E, $22^{\circ}37'18''$ S) (Figure 1A). The quarry exposes well-foliated granitic gneisses, Massive pegmatite and red-colored syenite (Figure 2A,B). The granitic gneisses experienced variable degrees of migmatization and are intruded by the pink pegmatite (Figure 2A). The syenite is profusely traversed by decimeter- to meter-sized veins of pegmatite, which is strongly deformed and fragmented (Figure 2B). Ten samples, including three biotite granitic gneisses, one syeno-granite, two syeno-granitic pegmatites, one syeno-granitic gneiss, one granitic syenite, and two biotite quartz monzonites, were collected for petrology and geochemistry, and, among them, three samples were sent for monazite U-Pb dating. A summary of petrology, geochemistry, and monazite results are given in the following sections.

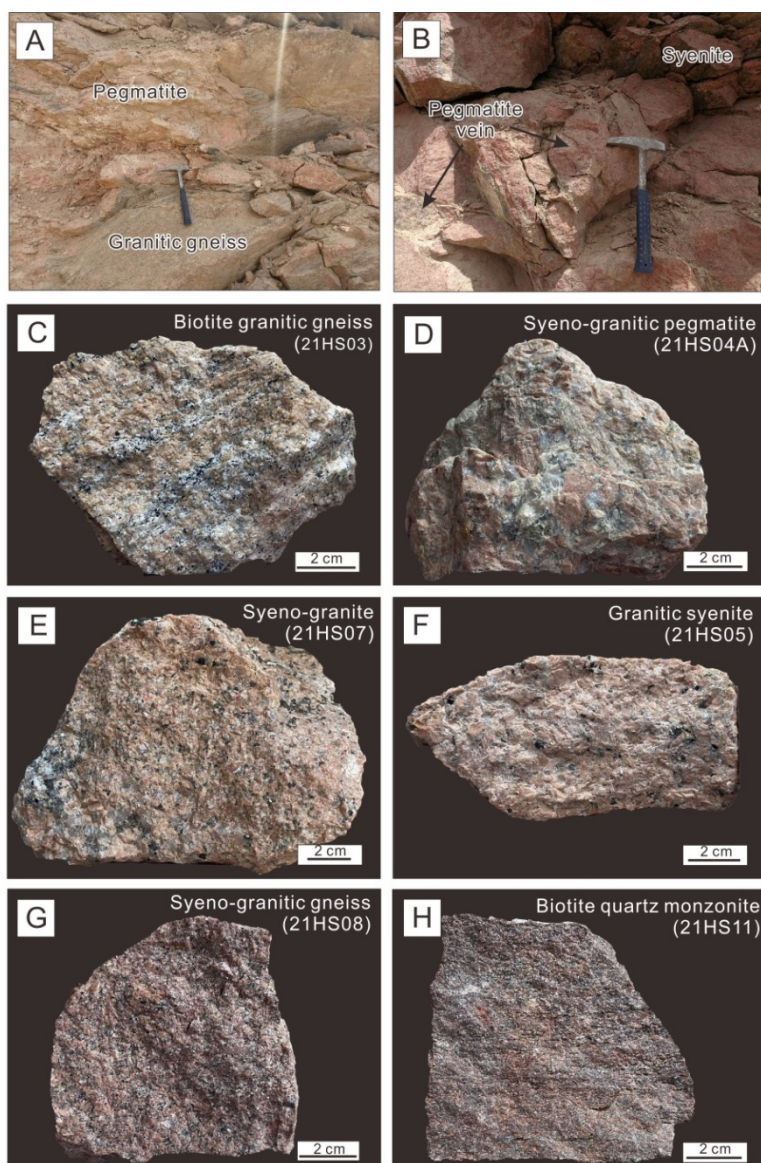


Figure 2. Representative hand specimen photographs of the AMC basement rocks. (A) Granitic gneisses are intruded by pink pegmatite; (B) syenite with pegmatite veins; (C) biotite granitic gneiss; (D) syeno-granitic pegmatite; (E) Syeno-granite; (F) granitic syenite; (G) syeno-granitic gneiss; (H) biotite quartz monzonite.

3. Analytical Techniques

3.1. Whole-Rock Geochemistry

The Major-element analysis of ten samples was carried out in the Yanduzhongshi Geological Analysis Laboratories Ltd., Beijing, China. Fresh samples were first crushed to centimeter sizes; only the fresh pieces were selected, washed with deionized water, dried, and then ground to less than 200 mesh (0.5200 ± 0.0001 g) for geochemical analyses. Sample powders were mixed with flux $\text{Li}_2\text{B}_4\text{O}_7$ (1:8) to make homogeneous glass disks at 1250°C using a V8C automatic fusion Machine produced by the Analymate Company in China. The bulk rock Major elements were analyzed using X-ray fluorescence spectrometry techniques (Zetium, PANalytical, XRF-1800, Shimadzu Corporation, Kyoto, Japan). The analytical errors for Major elements were better than 1%. Trace (including rare earth elements) element analyses of the sample were conducted in the National Research Center for Geoanalysis, Beijing. Trace element concentrations were determined as solute by Thermo fisher X-Series inductively coupled plasma Mass spectrometry (ICP-MS). About 25 mg of powder was

dissolved for about 48 h at 120 °C using 1 mL HF and 0.5 mL HNO₃ mixtures in screwtop Teflon beakers, followed by evaporation to dryness. The Material was re-dissolved in 2 mL 1:1 HNO₃ for 8 h at 120 °C [36]. The analytical errors are less than 10% depending on the concentration of any given element.

3.2. Monazite U-Pb Dating

U-Pb dating of monazite from three samples was conducted by LA-ICP-MS at the Wuhan Sample Solution Analytical Technology Co., Ltd., Wuhan, China. Laser sampling was performed using a GeolasPro laser ablation system that consists of a COMPexPro 102 ArF excimer laser (wavelength of 193 nm and Maximum energy of 200 mJ) and a MicroLas optical system. An Agilent 7700 e ICP-MS instrument was used to acquire ion-signal intensities. Helium was applied as a carrier gas. Argon was used as the Make-up gas and mixed with the carrier gas via a T-connector before entering the plasma ICP. A “wire” signal smoothing device is included in this laser ablation system, by which smooth signals are produced even at very low laser repetition rates down to 1 Hz [37]. It is very useful for in-situ U-Pb dating of high-U mineral [38]. The spot size and frequency of the laser were set to 16 μm and 2 Hz, respectively. Monazite standard 44,069 and glass NIST610 were used as external standards for U-Pb dating and trace element calibration, respectively. Each analysis incorporated a background acquisition of approximately 20–30 s followed by 50 s of data acquisition from the sample. An Excel-based software ICPMSDataCal 10.9 (China University of Geosciences, Wuhan, China) was used to perform off-line selection and integration of background and analyzed signals, time-drift correction, and quantitative calibration for trace element analysis and U-Pb dating [39,40]. Concordia diagrams and weighted mean calculations were Made using Isoplot/Ex_ver3 [41].

4. Results

4.1. Sample Description and Petrography

4.1.1. Biotite Granitic Gneiss

The biotite granitic gneisses (21HS01, 21HS02, 21HS03) are characterized by alternating biotite and plagioclase, along with pink alkaline feldspar leucosome with or without quartz vein, either formed as layering or heterogenous (Figure 2C). The biotite granitic gneisses are foliated and composed of fine- to medium-grained orthoclase (5–10%), perthitic orthoclase (5–10%), microcline (15–20%), plagioclase (15–20%), quartz (25–30%), biotite (5–10%), minor Magnetite (<5%) and calcite (Figure 3A–C). Accessory minerals include monazite, zircon, apatite, and uraninite. The gneissic fabric is defined by the alternating elongated quartz and feldspar layers with thinly biotite-bearing layers. Orthoclase is subhedral to anhedral and contains quartz inclusions. Microcline is anhedral and partly altered. Plagioclase is subhedral to anhedral, and some grains are rimmed by albite/quartz, indicating partial melting and dissolution [42,43]. Perthitic orthoclase is rimmed by albite showing rapakivi-like texture. Dissolution of albite between grain Margins is common. Quartz is recrystallized and elongated and contains microcline and perthitic orthoclase inclusions, and some grains exhibit rounded morphology.

4.1.2. Syeno-Granite and Syeno-Granitic Pegmatite

The syeno-granite (21HS07) and two syeno-granitic pegmatites (21HS04A, 21HS04B) are dominated by medium- to coarse- (0.5 cm to 1 cm) grained pink colored alkali feldspar and grey colored quartz, and minor opaque minerals (Figure 2D,E). The syeno-granite and two syeno-granitic pegmatites are composed of orthoclase (5–15%), perthitic orthoclase (10–25%), microcline (10–20%), plagioclase (5–10%), quartz (25–30%), biotite (<5%), and minor calcite and Magnetite (Figure 3D–G). Accessory minerals include zircon, monazite, apatite, and xenotime. Feldspar and quartz morphology are euhedral to subhedral in some areas, but also can be rounded and anhedral in other places. Microcline and plagioclase are partly sericitized. Some feldspar grains are perthitic orthoclase in the center and microcline at the Margin. Plagioclase is rimmed by albite/quartz, together with quartz showing

myrmekite texture. Recrystallized fine-grained quartz aggregates formed between coarse-grained orthoclase and perthitic orthoclase. Quartz forms as two types, either fine-grained rounded morphology or anhedral coarse-grained with embayed morphology, and locally contain microcline.

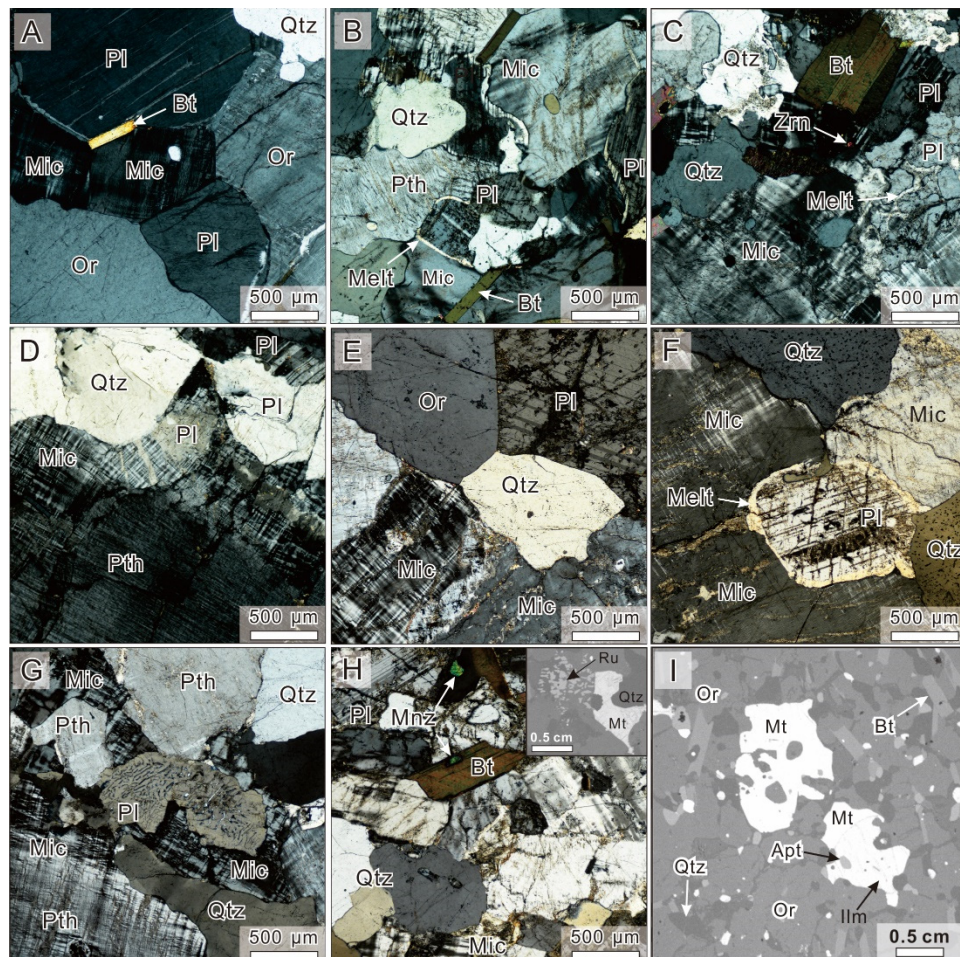


Figure 3. Representative photomicrographs of the AMC. (A–C) Biotite granitic gneiss; (D–G) syeno-granitic pegmatite; (H) syeno-granitic gneiss; (I) biotite quartz monzonite. (A–H) are cross-polarized light photos, and inset photo in (H,I) are backscattered photomicrographs. Mineral abbreviations: Pl—plagioclase, Or—orthoclase; Qtz—quartz; Mic—microcline, Pth—perthitic orthoclase; Bt—biotite; Mt—magnetite; Mnz—monazite; Zrn—zircon.

4.1.3. Syeno-Granitic Gneiss

The syeno-granitic gneiss (21HS08) is red colored, foliated, and composed of pink alkali feldspar and biotite (Figure 2G). The syeno-granitic gneiss is composed of fine-grained (up to 0.25 cm) orthoclase (10–15%), microcline (10–15%), perthitic/antiperthitic orthoclase (5–10%), plagioclase (10–15%), quartz (30–35%), biotite (5–10%), and minor Magnetite (<5%), as well as ilmenite (Figure 3H). Accessory minerals include zircon, monazite, apatite, and rutile. Orthoclase and quartz exhibit rounded or embayed morphology. Some of the plagioclase is rimmed by perthitic orthoclase/albite and interpreted as textural evidence of partial melting and dissolution.

4.1.4. Granitic Syenite

The granitic syenite (21HS05) is pink-colored and composed of alkaline feldspar, minor grey colored quartz, and opaque minerals (Figure 2F). The granitic syenite is composed of medium-grained (up to 0.25 cm) orthoclase (15–25%), perthitic orthoclase (10–20%),

microcline (20–30%), plagioclase (10–15%), quartz (5%), biotite (5%), and minor Magnetite. Accessory minerals include zircon, and monazite. All feldspar is subhedral to anhedral, and quartz exhibits anhedral morphology. Some quartz, orthoclase, and perthitic orthoclase exhibit dihedral angles, indicating textural equilibration. The coarse-grained perthitic orthoclase, microcline, and quartz exhibits embayed morphology with albite between these grain boundaries, indicating partial melting.

4.1.5. Biotite Quartz Monzonite

The biotite quartz monzonites (21HS09, 21HS11) are dominated by red alkaline feldspar and dark layers or pockets of Magnetite (Figure 2H). The biotite quartz monzonites are composed of fine-grained orthoclase (5–10%), perthitic orthoclase (5%), microcline (20–25%), plagioclase (20–30%), quartz (10–15%), Magnetite and ilmenite (5–10%), minor biotite (2%) and muscovite (<5%) (Figure 3I). Accessory minerals include zircon, monazite, apatite, and rutile. Orthoclase is subhedral to anhedral, and exhibits rounded or embayed morphology and is rimmed by albite/quartz. Quartz forms as two types of morphology, either as anhedral or rounded in shape. Orthoclase is slightly altered, and some grains are rimmed by an albite selvedge.

4.2. Geochemistry

4.2.1. Biotite Granitic Gneiss, Syeno-Granite, Syeno-Granitic Pegmatite, Syeno-Granitic Gneiss, and Granitic Syenite

The biotite granitic gneisses, syeno-granite, syeno-granitic pegmatites, and syeno-granitic gneiss show high concentrations for SiO_2 (68.03–75.57 wt.%), Al_2O_3 (12.80–14.98 wt.%), K_2O (5.28–8.06 wt.%), wide variation of Na_2O (1.95–3.10 wt.%), Fe_2O_3 (0.42–4.81 wt.%), low concentrations for MgO (0.18–1.12 wt.%), CaO (0.20–1.59 wt.%), MnO (0.01–0.06 wt.%), TiO_2 (0.04–0.44 wt.%) and P_2O_5 (0.06–0.18 wt.%) (Table 1). These rocks show high total alkali contents of 8.37–10.66 wt.% and corresponds to granite compositions (Figure 4A). In terms of alumina saturation index, they are peraluminous (A/CNK : 1.03–1.12) and show variations from alkali-calcic to alkalic with low Fe-number (Fe^* : 0.71–0.90) (Figure 4B–D). Chondrite-normalized rare earth element (REE) patterns of two biotite granitic gneisses and one syeno-granitic gneiss show pronounced LREE enrichment, HREE depletion and negative Eu anomalies (Eu/Eu^* : 0.26–0.37) with high ratios for $(\text{Gd/Yb})_{\text{N}}$: 2.4–6.3, $(\text{La/Yb})_{\text{N}}$: 18.9–33.0 and variable ratios for $(\text{La/Sm})_{\text{N}}$: 2.8–4.8 (Figure 5A). By contrast, the syeno-granite, syeno-granitic pegmatites and one biotite granitic gneiss are characterized by positive Eu anomalies (Eu/Eu^* : 1.31–1.94), relatively low REE abundance, and low ratios of $(\text{Gd/Yb})_{\text{N}}$: 0.4–1.8, $(\text{La/Yb})_{\text{N}}$: 0.7–16.6, $(\text{La/Sm})_{\text{N}}$: 1.6–6.1. Primitive Mantle-normalized trace element patterns reflect distinct negative anomalies at Nb-Ta, Ba, Sr, and Ti with distinct Th, U, and Pb enrichment (Figure 5B).

In contrast, the granitic syenite shows relatively lower SiO_2 (65.65 wt.%), Fe_2O_3 (0.38 wt.%), and Na_2O (1.50 wt.%), and higher Al_2O_3 (17.92 wt.%), K_2O (10.54 wt.%), and P_2O_5 (0.69 wt.%) than the rocks described above, and low concentrations for MgO (0.36 wt.%), CaO (1.31 wt.%), MnO (0.05 wt.%) and TiO_2 (0.08 wt.%). The total alkali content of 12.04 wt.% is higher than the rocks described above and corresponds to syenite composition (Figure 4A). The rock is alkalic and peraluminous (A/CNK : 1.10) with a low Fe-number (Fe^* : 0.63) (Figure 4B–D). Chondrite-normalized REE pattern for the granitic syenite shows flat REE pattern with low ratios for $(\text{Gd/Yb})_{\text{N}}$: 1.1, $(\text{La/Yb})_{\text{N}}$: 2.3, and $(\text{La/Sm})_{\text{N}}$: 1.9 (Figure 5A). The primitive Mantle-normalized trace element pattern reflects distinct negative anomalies at Nb, Ba, and Ti with U and Pb enrichment (Figure 5B).

Table 1. Whole-rock geochemical data for studied rock types from the Abbabis Metamorphic Complex.

Sample No.	21HS01	21HS02	21HS03	21HS04A	21HS04B	21HS07	21HS08	21HS05	21HS09	21HS11
Major elements (wt.%)										
SiO ₂	72.74	68.03	71.42	74.73	75.00	75.57	71.54	65.65	66.82	61.89
Al ₂ O ₃	14.13	14.29	14.98	13.21	14.05	12.80	14.11	17.92	14.28	13.73
Fe ₂ O ₃	1.97	4.81	1.55	0.58	0.42	1.47	2.70	0.38	3.46	7.97
CaO	1.59	1.37	0.65	0.39	1.15	0.20	1.11	1.31	0.66	2.03
MgO	0.55	1.12	0.65	0.28	0.21	0.18	0.60	0.36	0.77	0.48
K ₂ O	5.28	6.56	8.06	7.49	6.67	7.78	6.28	10.54	8.89	7.38
Na ₂ O	3.10	2.47	2.60	2.69	2.34	1.95	2.28	1.50	1.45	0.73
TiO ₂	0.15	0.40	0.14	0.04	0.04	0.08	0.44	0.08	1.10	1.51
P ₂ O ₅	0.06	0.09	0.06	0.07	0.06	0.08	0.18	0.69	0.39	1.00
LOI	0.62	0.80	0.35	0.47	0.48	0.23	0.62	0.32	0.34	0.37
Total	100.17	99.95	100.46	99.94	100.43	100.33	99.85	98.75	98.17	97.10
Trace elements (ppm)										
V	33.06	67.11	13.94	10.36	5.53	17.50	33.25	12.55	86.32	120.00
Ba	379.5	680.4	626.8	300	1129	986.3	796.8	3167	2344	969.2
Gd	7.545	21.689	1.798	1.901	1.370	1.159	17.31	6.88	16.04	20.34
Ni	3.167	9.004	3.558	1.741	1.466	0.947	2.416	2.259	8.573	6.116
Zn	23.2	57.1	24.8	6.0	13.9	14.1	40.4	18.2	59.8	42.4
Cr	2.54	20.17	3.02	2.16	2.03	2.14	5.43	3.24	7.64	13.93
Pb	47.76	57.79	55.15	17.29	39.73	41.24	39.9	50.64	44.17	26.8
Li	14.63	25.44	16.63	1.991	7.687	5.891	12.7	6.923	11.34	8.726
Be	1.56	1.329	1.069	2.568	2.311	1.679	2.073	1.776	1.2	1.618
Sc	24.62	18.86	10.19	14.45	11.22	11.45	9.70	27.81	17.25	22.65
Co	2.543	5.698	2.326	0.999	1.002	1.372	2.553	1.572	7.943	4.223
Ga	18.07	25.59	16.94	11.88	13.77	13.62	18.11	17.36	21.76	20.32
Rb	301.7	413.2	425.6	412.4	297.1	405.4	322.7	473.5	450.7	326.3
Sr	75.8	97.6	110.1	69.3	150.9	91.7	103.1	186.5	110.9	128
Y	33.31	80.20	13.71	17.92	6.54	7.56	34.46	50.55	54.87	62.02
Zr	156.5	295.6	42.2	39.8	35.2	68.6	283.9	42.9	342.6	393.5
Nb	8.56	17.57	9.59	74.96	2.75	6.01	19.42	7.52	42.70	45.82
Sn	3.342	7.621	4.146	1.748	0.812	1.696	4.681	1.524	8.963	4.776
Cs	2.56	4.201	3.214	8.566	2.814	6.748	3.404	5.495	3.919	2.255
La	67.79	149.1	17.27	4.202	14.4	8.971	104.4	17.57	115.1	150.9
Ce	120.7	279.4	28.05	10.43	26.63	14.64	224.1	34.69	227.3	274.7
Pr	13.67	44.83	2.826	1.164	2.747	1.645	39.29	4.973	39.18	45.91
Nd	45.57	148.8	9.31	4.88	9.53	5.67	139.5	20.32	132.2	159.3
Sm	9.128	25.81	1.813	1.674	1.667	1.155	23.79	5.962	20.50	24.44
Eu	0.873	2.028	0.780	0.214	0.986	0.619	1.385	1.838	3.450	4.248
Tb	1.271	3.265	0.332	0.458	0.242	0.2	2.185	1.32	2.294	2.702
Dy	6.487	15.82	2.069	3.565	1.331	1.277	8.713	8.921	10.85	12.58
Ho	1.249	2.844	0.46	0.796	0.251	0.277	1.345	1.909	2.044	2.264
Er	3.451	7.843	1.557	2.917	0.771	0.926	3.703	6.057	6.094	6.879
Tm	0.420	0.888	0.231	0.521	0.096	0.140	0.382	0.863	0.778	0.830
Yb	2.578	5.248	1.664	4.073	0.624	0.936	2.271	5.371	5.256	5.505
Lu	0.371	0.677	0.245	0.569	0.089	0.16	0.326	0.702	0.754	0.796
Hf	5.412	12.28	1.554	2.329	1.481	2.203	11.42	1.496	12.67	13.16
Ta	0.438	1.038	0.534	10.264	0.282	0.886	1.331	0.904	4.115	2.552
Tl	1.186	1.742	1.791	1.64	1.21	1.635	1.349	2.12	1.692	1.338
Th	66.14	105.8	14.66	24.07	7.039	3.83	110.8	2.658	61.26	17.88
U	4.534	10.82	2.693	38.3	4.755	1.102	4.627	1.444	7.444	5.706
REE	281.10	708.24	68.40	37.36	60.74	37.77	568.70	117.37	581.84	711.39
δEu	0.31	0.26	1.31	0.37	1.94	1.62	0.20	0.87	0.56	0.57
(La/Sm) _N	4.8	3.7	6.1	1.6	5.6	5.0	2.8	1.9	3.6	4.0
(La/Yb) _N	18.9	20.4	7.4	0.7	16.6	6.9	33.0	2.3	15.7	19.7
(Gd/Yb) _N	2.4	3.4	0.9	0.4	1.8	1.0	6.3	1.1	2.5	3.1

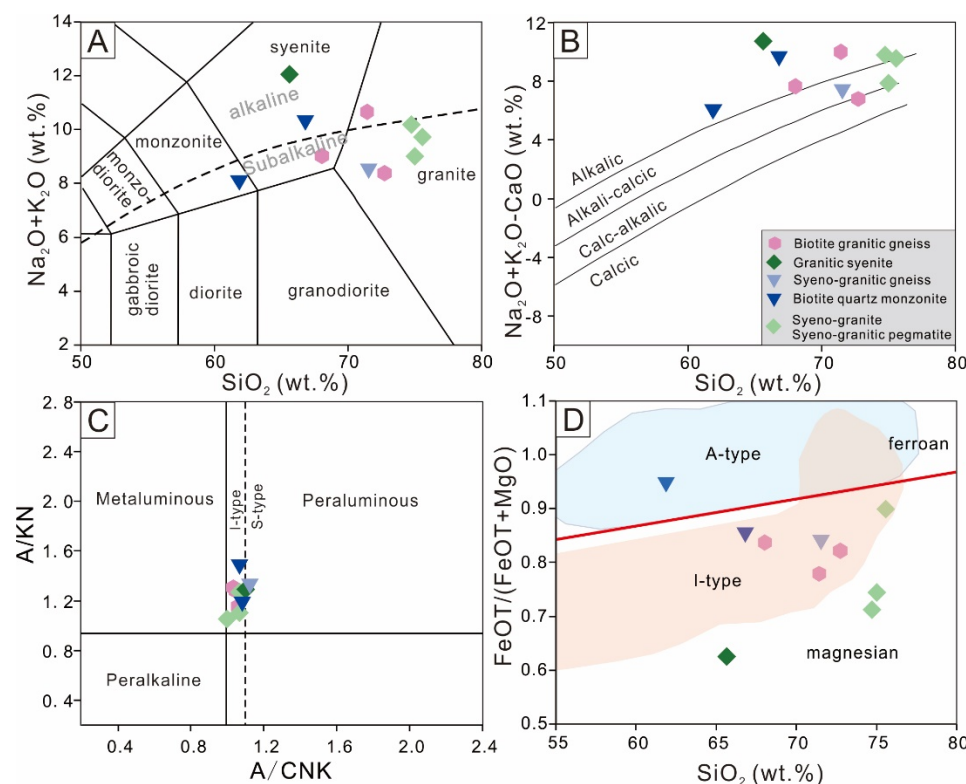


Figure 4. Geochemical classification plots of the biotite granitic gneiss, syeno-granite, syeno-granitic pegmatite, syeno-granitic gneiss, granitic syenite, and biotite quartz monzonite. (A) Total alkalis vs. silica plot [44]. (B) $(\text{Na}_2\text{O} + \text{K}_2\text{O} - \text{CaO}) - \text{SiO}_2$ [45] classification diagram showing potassian contents and calcic to alkalic. (C) A/NK [molar Al_2O_3]/($\text{Na}_2\text{O} + \text{K}_2\text{O}$) vs. A/CNK [molar Al_2O_3]/($\text{CaO} + \text{Na}_2\text{O} + \text{K}_2\text{O}$) for evaluating peralkaline, metaluminous, and peraluminous melt compositions [46]. (D) $\text{FeOT}/(\text{FeOT} + \text{MgO}) - \text{SiO}_2$ showing ferroan and Magnesian [45].

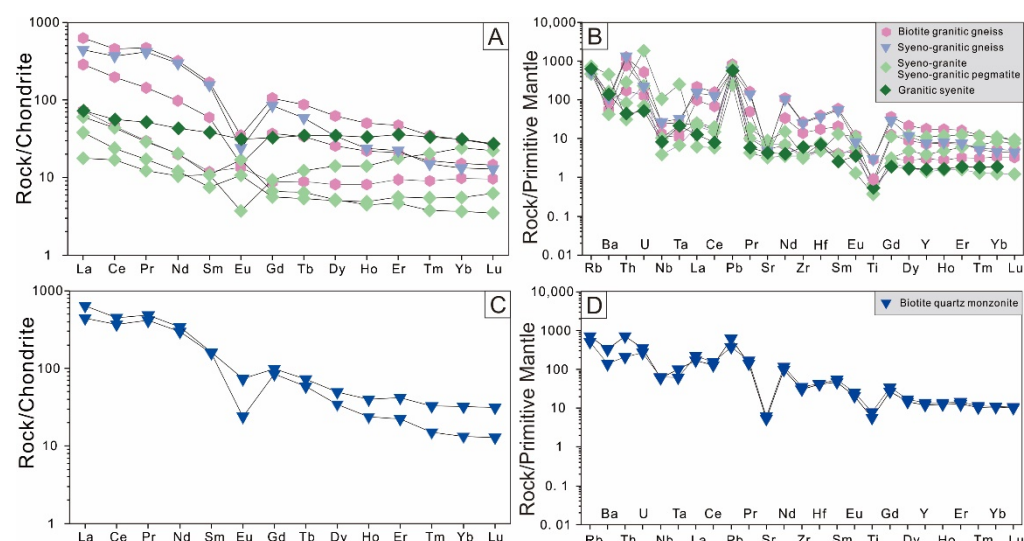


Figure 5. (A,C) chondrite-normalized REE patterns, (B,D) primitive Mantle-normalized trace element abundance patterns (B,D). Both chondrite- and primitive-normalization values are taken from Sun and McDonough [47].

4.2.2. Biotite Quartz Monzonite

Major oxide compositions for the biotite quartz monzonites are characterized by less SiO_2 (61.89–66.82 wt.%) and Na_2O (0.73–1.45 wt.%), higher Fe_2O_3 (3.46–7.97 wt.%),

TiO_2 (1.10–1.51 wt.%) and MnO (0.07 wt.%) than the rocks described above, high Al_2O_3 (13.73–14.28 wt.%) and K_2O (7.38–8.89 wt.%), and low CaO (0.66–2.03 wt.%), P_2O_5 (0.39–1.00 wt.%) and MgO (0.48–0.77 wt.%) contents (Table 1). The biotite quartz monzonites correspond to syenite and quartz monzonite compositions (Figure 4A). Those rocks are alkalic and peraluminous (A/CNK : 1.07–1.08) with low Fe-number (Fe^* : 0.86–0.95) (Figure 4B–D). Chondrite-normalized REE patterns for the biotite quartz monzonite show pronounced LREE enrichment, depleted HREE pattern, and negative Eu anomalies (Eu/Eu^* : 0.56–0.57) with high $(\text{La}/\text{Sm})_{\text{N}}$: 3.6–4.0, $(\text{La}/\text{Yb})_{\text{N}}$: 15.7–19.7 and $(\text{Gd}/\text{Yb})_{\text{N}}$: 2.5–3.1 (Figure 5A). Primitive Mantle-normalized trace element patterns reflect distinct negative anomalies at Nb-Ta, Ba, Sr, and Ti with distinct Th, U, and Pb enrichment (Figure 5B).

4.3. Monazite U-Pb Geochronology

Three samples were dated for monazite U–Pb geochronology, including biotite granitic gneiss, syeno-granite, and syeno-granitic pegmatite, with all monazite data given in Table 2 and morphology shown in Figure 6 and data plotted in Figure 7.

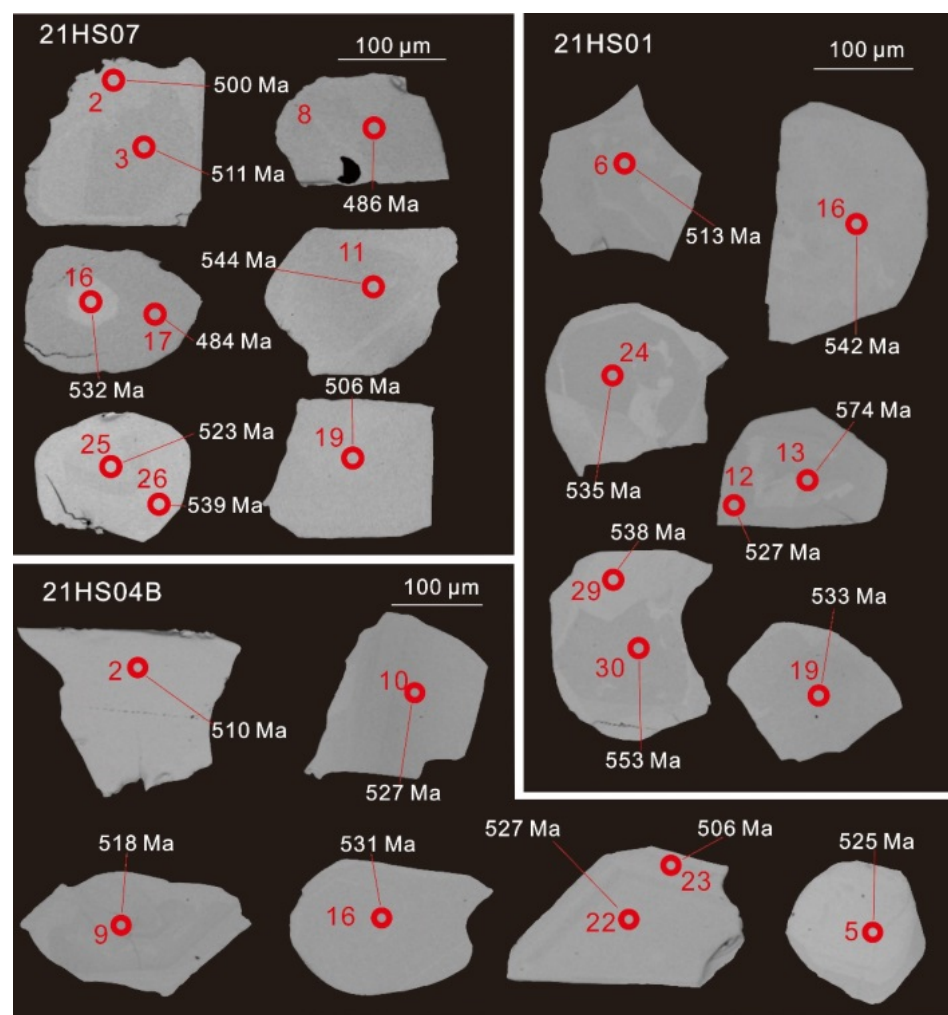


Figure 6. Representative Cathodoluminescence (CL) images of monazite grains from biotite granitic gneiss (21HS01), syeno-granite (21HS07), and syeno-granitic pegmatite (21HS04B).

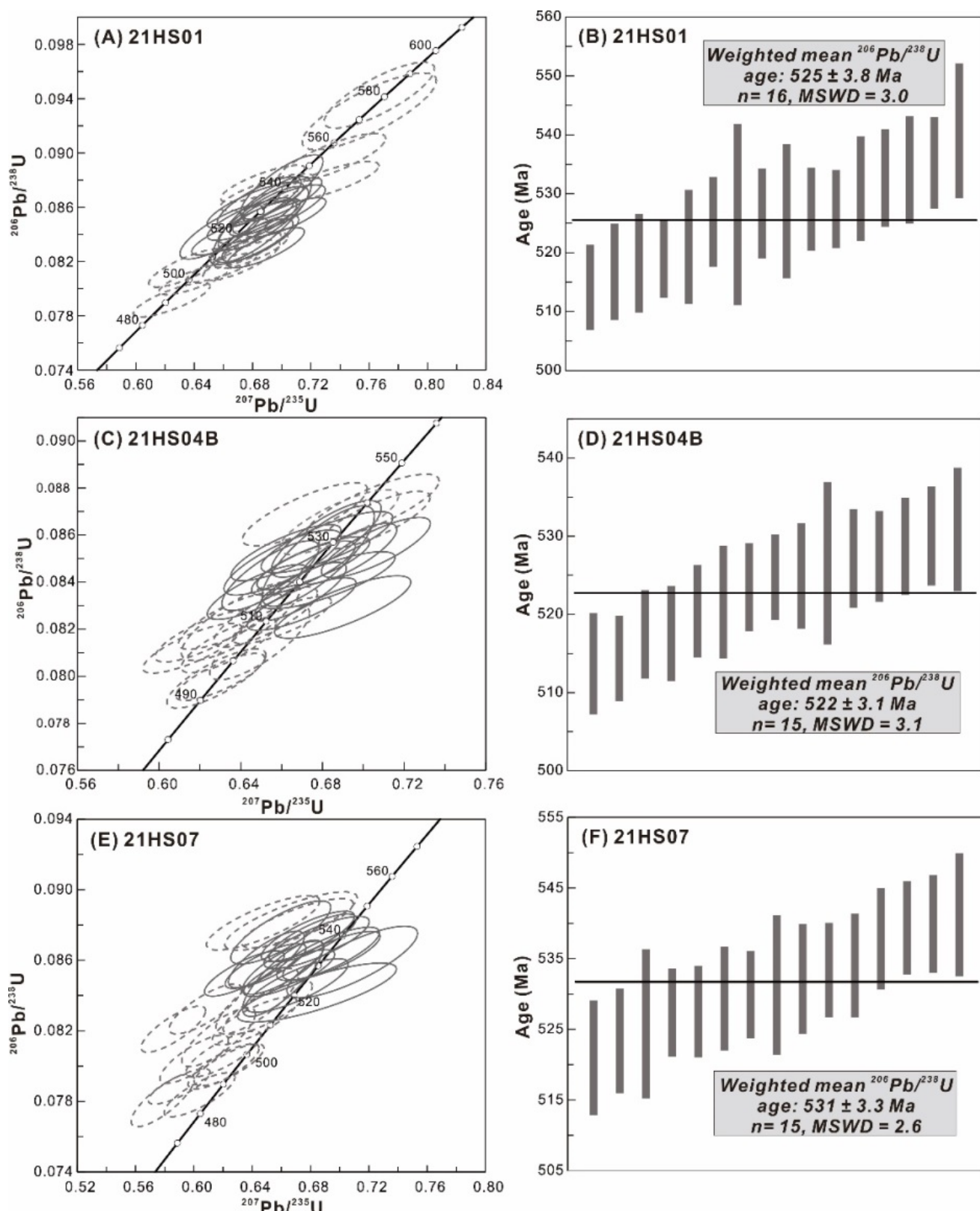


Figure 7. Wetherill U-Pb concordia plots and weighted average plots: (A,B) for biotite granitic gneiss (21HS01); (C,D) for syeno-granitic pegmatite (21HS04B); (E,F) for syeno-granite (21HS07).

Table 2. LA-ICP-MS monazite age data from the Abbabis Metamorphic Complex.

Sample No.	Th (ppm)	U (ppm)	Th/U	Isotopic Ratios						Age (Ma)			
				$^{207}\text{Pb}/^{206}\text{Pb}$		$^{207}\text{Pb}/^{235}\text{U}$		$^{206}\text{Pb}/^{238}\text{U}$		$^{207}\text{Pb}/^{206}\text{Pb}$		$^{207}\text{Pb}/^{235}\text{U}$	
				Ratio	1σ	Ratio	1σ	Ratio	1σ	Age	1σ	Age	1σ
21HS01-05	116,640	4232	27.6	0.0572	0.0010	0.6245	0.0107	0.0792	0.0005	502	39	493	7
21HS01-04	138,515	5556	24.9	0.0575	0.0009	0.6404	0.0101	0.0807	0.0005	522	35	503	6
21HS01-21	126,558	4360	29.0	0.0564	0.0010	0.6352	0.0107	0.0815	0.0006	478	37	499	7
21HS01-02	144,048	8036	17.9	0.0585	0.0009	0.6588	0.0097	0.0815	0.0004	550	36	514	6
21HS01-01	117,932	5113	23.1	0.0594	0.0010	0.6723	0.0108	0.0821	0.0006	589	37	522	7
21HS01-26	95,643	5271	18.1	0.0594	0.0009	0.6790	0.0103	0.0828	0.0005	589	31	526	6
21HS01-06	143,917	6408	22.5	0.0590	0.0009	0.6739	0.0103	0.0829	0.0005	565	33	523	6
21HS01-28	122,865	5553	22.1	0.0602	0.0010	0.6890	0.0108	0.0830	0.0006	613	40	532	7
21HS01-18	130,995	5038	26.0	0.0590	0.0011	0.6793	0.0116	0.0835	0.0007	569	39	526	7
21HS01-25	121,006	8558	14.1	0.0594	0.0009	0.6853	0.0107	0.0837	0.0007	589	33	530	6
21HS01-20	157,779	5226	30.2	0.0574	0.0010	0.6645	0.0107	0.0838	0.0006	506	32	517	7
21HS01-11	133,428	5138	26.0	0.0568	0.0010	0.6590	0.0118	0.0842	0.0008	483	34	514	7
21HS01-22	130,322	3995	32.6	0.0584	0.0010	0.6835	0.0110	0.0849	0.0006	546	37	529	7
21HS01-15	111,605	3981	28.0	0.0588	0.0012	0.6866	0.0137	0.0851	0.0013	561	47	531	8
21HS01-17	136,888	3260	42.0	0.0577	0.0010	0.6785	0.0121	0.0851	0.0006	517	44	526	7
21HS01-12	117,675	5412	21.7	0.0586	0.0010	0.6873	0.0126	0.0852	0.0010	550	34	531	8
21HS01-23	88,343	3554	24.9	0.0598	0.0010	0.7029	0.0112	0.0852	0.0006	598	37	541	7
21HS01-03	155,462	4841	32.1	0.0586	0.0009	0.6885	0.0100	0.0853	0.0006	550	33	532	6
21HS01-10	109,788	3506	31.3	0.0591	0.0011	0.6981	0.0130	0.0858	0.0007	569	41	538	8
21HS01-19	72,105	2841	25.4	0.0574	0.0012	0.6819	0.0135	0.0861	0.0007	509	46	528	8
21HS01-07	120,720	4330	27.9	0.0576	0.0010	0.6846	0.0118	0.0864	0.0008	522	37	530	7
21HS01-24	109,422	4461	24.5	0.0586	0.0009	0.7002	0.0112	0.0866	0.0007	554	35	539	7
21HS01-29	149,214	3185	46.9	0.0574	0.0011	0.6897	0.0131	0.0871	0.0006	506	41	533	8
21HS01-14	156,034	7401	21.1	0.0581	0.0010	0.7000	0.0116	0.0875	0.0010	600	35	539	7
21HS01-16	102,901	3071	33.5	0.0567	0.0010	0.6872	0.0119	0.0877	0.0006	480	39	531	7
21HS01-27	132,695	2053	64.6	0.0604	0.0012	0.7324	0.0140	0.0879	0.0006	620	43	558	8
21HS01-30	97,096	3156	30.8	0.0595	0.0013	0.7346	0.0150	0.0896	0.0007	587	46	559	9
21HS01-13	147,529	1343	109.8	0.0593	0.0014	0.7600	0.0188	0.0931	0.0012	589	50	574	11
21HS01-09	105,176	2632	40.0	0.0590	0.0011	0.7669	0.0155	0.0943	0.0010	569	39	578	9
21HS04B-30	81,493	5422	15.0	0.0570	0.0009	0.6280	0.0099	0.0799	0.0005	500	35	495	6
21HS04B-29	64,615	6692	9.7	0.0570	0.0008	0.6299	0.0089	0.0800	0.0004	494	31	496	6
21HS04B-27	73,748	3501	21.1	0.0550	0.0009	0.6163	0.0099	0.0812	0.0004	413	37	488	6
21HS04B-26	73,491	5702	12.9	0.0565	0.0009	0.6341	0.0095	0.0813	0.0005	478	33	499	6
21HS04B-15	74,376	6044	12.3	0.0578	0.0009	0.6492	0.0100	0.0814	0.0006	524	40	508	6
21HS04B-23	80,529	6968	11.6	0.0551	0.0009	0.6217	0.0097	0.0817	0.0004	417	31	491	6
21HS04B-14	1299	2838	0.5	0.0564	0.0011	0.6399	0.0119	0.0823	0.0007	478	38	502	7
21HS04B-21	84,466	5594	15.1	0.0559	0.0009	0.6349	0.0104	0.0824	0.0005	456	37	499	6
21HS04B-02	68,192	5610	12.2	0.0581	0.0009	0.6601	0.0099	0.0824	0.0004	532	33	515	6
21HS04B-20	81,726	7007	11.7	0.0572	0.0009	0.6521	0.0104	0.0825	0.0005	498	33	510	6
21HS04B-06	79,190	3712	21.3	0.0601	0.0011	0.6899	0.0136	0.0829	0.0005	609	44	533	8
21HS04B-08	83,089	4995	16.6	0.0584	0.0010	0.6698	0.0109	0.0831	0.0005	546	40	521	7
21HS04B-28	70,791	6247	11.3	0.0562	0.0009	0.6483	0.0101	0.0836	0.0005	461	31	507	6
21HS04B-09	64,534	6241	10.3	0.0580	0.0008	0.6692	0.0092	0.0836	0.0005	528	31	520	6
21HS04B-25	60,643	2750	22.1	0.0588	0.0012	0.6826	0.0135	0.0841	0.0005	561	44	528	8
21HS04B-17	71,079	5989	11.9	0.0563	0.0009	0.6545	0.0097	0.0843	0.0006	465	33	511	6
21HS04B-12	81,809	5436	15.0	0.0574	0.0009	0.6707	0.0104	0.0846	0.0005	509	35	521	6
21HS04B-05	82,012	5134	16.0	0.0577	0.0010	0.6756	0.0113	0.0848	0.0005	517	37	524	7
21HS04B-19	79,959	3478	23.0	0.0564	0.0010	0.6604	0.0117	0.0848	0.0006	465	39	515	7
21HS04B-13	77,038	5367	14.4	0.0580	0.0010	0.6779	0.0112	0.0851	0.0009	528	41	526	7
21HS04B-10	70,747	6129	11.5	0.0589	0.0009	0.6925	0.0098	0.0852	0.0005	565	33	534	6
21HS04B-22	69,534	3796	18.3	0.0563	0.0009	0.6621	0.0110	0.0853	0.0005	461	32	516	7
21HS04B-04	80,682	3483	23.2	0.0599	0.0010	0.7062	0.0109	0.0855	0.0005	611	35	542	7
21HS04B-07	85,820	3463	24.8	0.0577	0.0012	0.6822	0.0132	0.0857	0.0005	520	44	528	8
21HS04B-16	71,091	4609	15.4	0.0576	0.0009	0.6819	0.0110	0.0858	0.0007	522	35	528	7
21HS04B-01	74,996	3064	24.5	0.0577	0.0011	0.6880	0.0119	0.0866	0.0006	520	45	532	7
21HS04B-11	79,347	3454	23.0	0.0590	0.0010	0.7056	0.0111	0.0866	0.0005	569	40	542	7
21HS04B-24	73,530	3322	22.1	0.0559	0.0010	0.6714	0.0125	0.0869	0.0005	450	45	522	8
21HS04B-18	68,554	3057	22.4	0.0586	0.0011	0.7046	0.0133	0.0872	0.0006	550	41	542	8
21HS07-17	3122	4943	0.6	0.0537	0.0009	0.5786	0.0088	0.0781	0.0006	367	37	464	6
21HS07-08	6548	4355	1.5	0.0558	0.0009	0.6039	0.0099	0.0784	0.0005	456	35	480	6
21HS07-09	76,829	5716	13.4	0.0542	0.0008	0.5899	0.0087	0.0789	0.0004	389	33	471	6
21HS07-05	10,317	5498	1.9	0.0562	0.0009	0.6204	0.0099	0.0800	0.0005	461	31	490	6
21HS07-30	97,505	5996	16.3	0.0565	0.0009	0.6242	0.0097	0.0801	0.0005	472	35	492	6
21HS07-10	91,438	5171	17.7	0.0541	0.0008	0.6003	0.0096	0.0804	0.0006	372	35	477	6
21HS07-02	40,389	4156	9.7	0.0557	0.0010	0.6202	0.0105	0.0807	0.0005	443	6	490	7
21HS07-19	81,742	5678	14.4	0.0547	0.0009	0.6169	0.0103	0.0816	0.0007	398	37	488	6
21HS07-12	77,128	5138	15.0	0.0517	0.0008	0.5859	0.0090	0.0821	0.0005	272	37	468	6
21HS07-03	3860	3500	1.1	0.0563	0.0011	0.6416	0.0119	0.0826	0.0006	465	36	503	7
21HS07-15	84,257	4145	20.3	0.0528	0.0008	0.6078	0.0101	0.0832	0.0006	320	42	482	6
21HS07-24	79,311	3681	21.5	0.0566	0.0011	0.6507	0.0125	0.0833	0.0006	476	44	509	8
21HS07-23													

Table 2. Cont.

Sample No.	Th (ppm)	U (ppm)	Th/U	Isotopic Ratios								Age (Ma)			
				$^{207}\text{Pb}/^{206}\text{Pb}$		$^{207}\text{Pb}/^{235}\text{U}$		$^{206}\text{Pb}/^{238}\text{U}$		$^{207}\text{Pb}/^{206}\text{Pb}$		$^{207}\text{Pb}/^{235}\text{U}$		$^{206}\text{Pb}/^{238}\text{U}$	
				Ratio	1σ	Ratio	1σ	Ratio	1σ	Age	1σ	Age	1σ	Age	1σ
21HS07-22	81,133	3856	21.0	0.0559	0.0010	0.6614	0.0114	0.0856	0.0006	450	37	515	7	529	4
21HS07-14	81,362	3630	22.4	0.0549	0.0010	0.6491	0.0113	0.0857	0.0005	409	45	508	7	530	3
21HS07-21	68,689	3037	22.6	0.0595	0.0014	0.7086	0.0183	0.0859	0.0008	587	18	544	11	531	5
21HS07-16	85,868	3416	25.1	0.0547	0.0010	0.6497	0.0106	0.0861	0.0007	467	39	508	7	532	4
21HS07-28	78,444	3091	25.4	0.0584	0.0012	0.6942	0.0136	0.0863	0.0006	546	46	535	8	533	3
21HS07-29	78,662	2865	27.5	0.0580	0.0012	0.6920	0.0144	0.0864	0.0006	532	43	534	9	534	4
21HS07-01	79,454	2985	26.6	0.0569	0.0012	0.6842	0.0148	0.0870	0.0006	500	79	529	9	538	4
21HS07-26	77,621	3544	21.9	0.0565	0.0010	0.6815	0.0122	0.0873	0.0006	472	39	528	7	539	3
21HS07-07	72,621	3077	23.6	0.0563	0.0011	0.6782	0.0131	0.0874	0.0006	461	43	526	8	540	3
21HS07-18	82,503	2310	35.7	0.0547	0.0012	0.6596	0.0140	0.0876	0.0007	398	52	514	9	541	4
21HS07-06	85,569	1709	50.1	0.0553	0.0013	0.6710	0.0156	0.0881	0.0006	433	54	521	10	544	3
21HS07-11	80,774	2123	38.0	0.0532	0.0013	0.6475	0.0159	0.0881	0.0006	345	54	507	10	544	4
21HS07-04	87,549	1302	67.2	0.0547	0.0015	0.6666	0.0186	0.0882	0.0007	398	56	519	11	545	4

Monazite grains in sample 21HS01 are angular or round, and up to 150 μm in length. The grains are either homogenous in CL, or show core–rim internal structures and some grains contain abundant inclusions in the core (Figure 6). Twenty-nine spots were analyzed on twenty-six grains and show $^{206}\text{Pb}/^{238}\text{U}$ ages of 581–491 Ma with 6 older grains showing $^{206}\text{Pb}/^{238}\text{U}$ ages of 581–538 Ma; 7 spots yield younger ages of 513–491 Ma, and the remaining 16 spots yielded a concordant weighted mean $^{206}\text{Pb}/^{238}\text{U}$ age of 525 ± 3.8 Ma (MSWD = 3.0, $n = 16$) (Figure 7A,B).

Monazite grains in sample 21HS04B are angular or round, with lengths of 100–200 μm . Most grains are unzoned, and minor grains show core–rim structures (Figure 6). Twenty-nine spots were selected from 26 monazite grains for U–Pb analysis, and all data clusters between 539–496 Ma with 4 older grains showing $^{206}\text{Pb}/^{238}\text{U}$ ages of 539–535 Ma, 10 spots yield younger ages of 511–496 Ma, and the remaining 15 spots yield a concordant weighted mean $^{206}\text{Pb}/^{238}\text{U}$ age of 522 ± 3.1 Ma (MSWD = 3.1, $n = 15$) (Figure 7C,D).

Monazite grains from sample 21HS07 are angular or rounded in shape and up to 220 μm in length. Most of the grains are structureless and some grains show core–rim structures with the slightly dark cores surrounded by light rims (Figure 6). Thirty-one spots were analyzed on 23 grains, of which $^{206}\text{Pb}/^{238}\text{U}$ ages are clustered between 545–484 Ma, with 3 older grains showing $^{206}\text{Pb}/^{238}\text{U}$ ages of 545–544 Ma, 13 spots yield younger ages of 518–484 Ma, and the remaining 15 grains yield a concordant weighted mean age of 531 ± 3.3 Ma (MSWD = 2.6, $n = 15$) (Figure 7E,F).

5. Discussion

5.1. Petrogenesis Fractional Crystallization and Partial Melting

The biotite granitic gneisses, syeno-granite, syeno-granitic pegmatites, syeno-granitic gneiss, and granitic syenite are characterized by high SiO₂, Al₂O₃, and K₂O, moderate Na₂O, low CaO, Fe₂O₃, MgO, and MnO, and TiO₂ abundance. The alkali-calcic to alkalic and low Fe number characteristic suggest an igneous source resembling an I-type granite formed in an active continental Margin setting [48]. However, their K-rich nature and high K₂O/Na₂O (1.7–4.0) ratios, and peraluminous (A/CNK: 1.03–1.12) characters similar to an Al-rich sedimentary source and correspond to S-type granite rather than the peralkaline A-type granite [6]. In contrast, the biotite quartz monzonites are alkalic and peraluminous, and characterized by relatively lower SiO₂ and Na₂O, elevated Fe₂O₃ and TiO₂ abundance, higher K₂O/Na₂O (6.1–10.1) ratios than the rocks described above, which together with the abundance of muscovite, indicate a sedimentary source and resemble S-type granites (Figure 8A–H). On the CaO/(FeO^T + MgO + TiO₂) versus CaO + FeO^T + MgO + TiO₂ diagram, the granitic and syeno-granitic rocks plot in the greywacke and pelite fields, which suggests that the parent Magma has a sedimentary source contribution [49] (Figure 8I). In terms of high-field strength elements (HFSE), all these samples are characterized by pronounced negative anomalies at Nb-Ta, and Ti further support a calc-alkaline Magma source (Figure 5). Thus, the parent Magma for the granitic gneiss and syeno-granitic rocks,

granitic syenite and biotite quartz monazites, was derived from a mixed igneous and metasedimentary source.

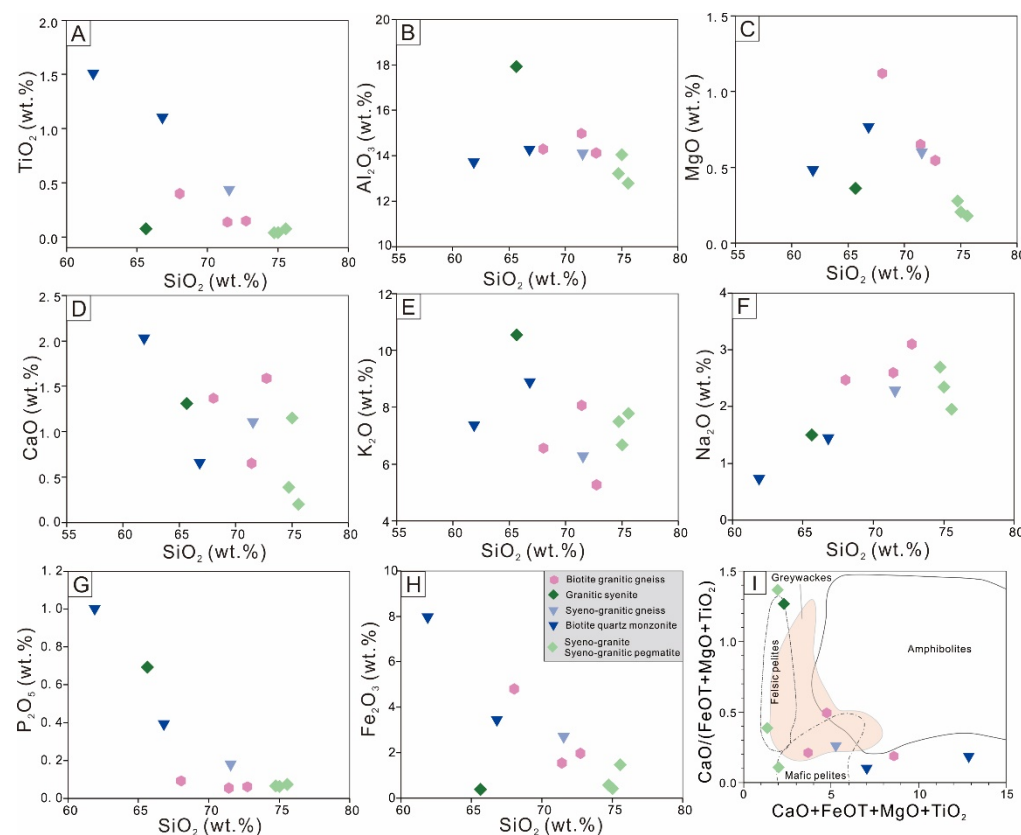


Figure 8. (A–H) SiO₂ vs. selected Major elements showing variation trends of biotite granitic gneiss, syeno-granite, syeno-granitic pegmatite, granitic syenite, syeno-granitic gneiss, and botite quartz monzonite. (I) CaO/(FeOT + MgO + TiO₂) – CaO + FeOT + MgO + TiO₂ diagram for discriminating melt sources from amphibolites, greywackes, Mafic/felsic pelites [49].

The granitic gneiss and syeno-granitic rocks, granitic syenite and biotite quartz monzonite, are characterized by negative Eu, Sr, and Ba anomalies, which indicate plagioclase and K-feldspar fractionation [50,51]. Depletion in the HREE and high (La/Yb)_N ratios suggest a high degree of fractionation of the parent Magma with residual garnet (Figure 5). One biotite granitic gneiss and two syeno-granitic pegmatites exhibit positive Eu anomalies and HREE enrichment features, indicating the absence of plagioclase fractional crystallization. Plagioclase fractional crystallization is also supported by the negative correlation of Sr and Eu versus SiO₂ and positive correlation of Na₂O versus SiO₂ (Figure 9A–H). Low abundance in P₂O₅ and Zr, and negative correlation of P₂O₅ and TiO₂ versus SiO₂ are explained by the moderate to abundant titanite, apatite and zircon. Negative correlation of CaO, MgO, Fe₂O₃, Co, and Ni versus SiO₂ indicates pyroxene and amphibole residue in the early crystallization stage. High K₂O and low MgO, Ni, and Co, and Cr abundance, and negative correlation of Rb, Sr, La, and V versus SiO₂ suggest that the Magma is highly evolved. The granitic gneiss and syeno-granitic rocks, granitic syenite and biotite quartz monzonite, are characterized by variable (La/Yb)_N ratios, indicating that the Magma has a high degree of fractionation.

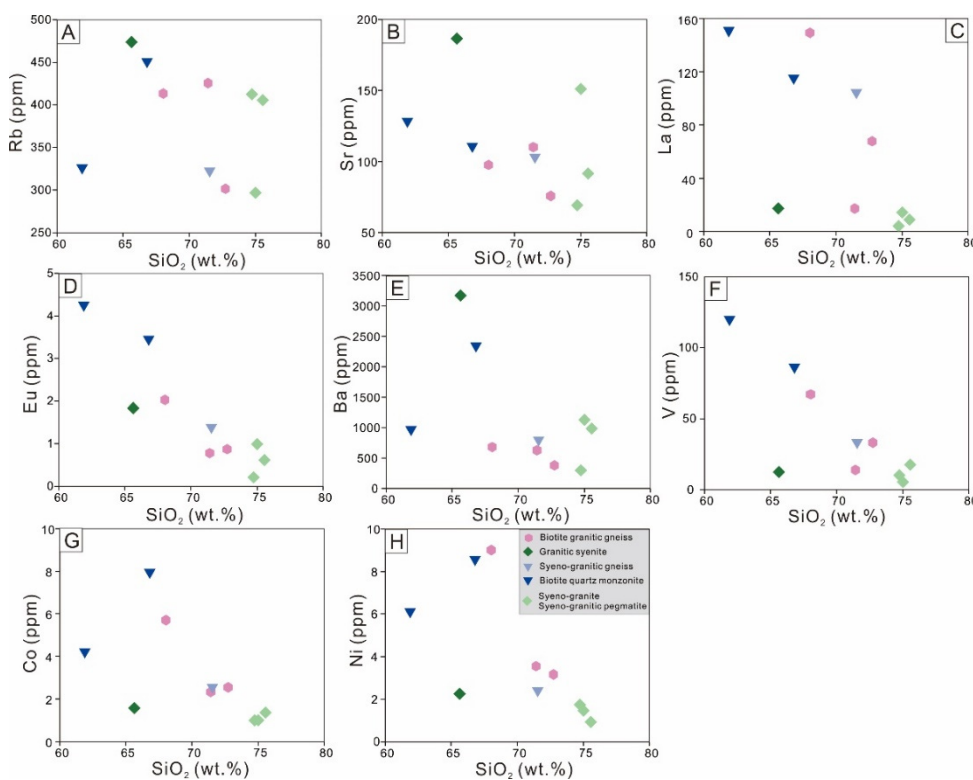


Figure 9. (A–H) SiO₂ vs. selected trace elements showing variation trends of biotite granitic gneiss, syeno-granite, syeno-granitic pegmatite, granitic syenite, syeno-granitic gneiss, and biotite quartz monzonite.

The fractionation crystallization model is further supported by the compatible (e.g., V, Ni) versus incompatible (e.g., Rb) element classification diagrams. These samples dominantly plot along the decreasing trend of compatible elements versus incompatible elements (Figure 10A,B). However, the studied samples exhibit a variable increasing trend of La/Sm and La/Yb ratios versus La abundance, suggesting these samples experienced variable degrees of partial melting, which is also consistent with the petrographic observation (Figure 10C,D). Kröner et al. [21] and Hawkeworth et al. [52] proposed that the late Paleoproterozoic pre-Damara basement experienced high degrees of partial melting during the late Neoproterozoic Damara Orogenic event. Therefore, we suggest that partial melting of the granitic gneiss and syeno-granitic rocks, granitic syenite and biotite quartz monazite occurred after crystallization of the rock.

In the (Na₂O + K₂O)/CaO versus 10,000Ga/Al diagram, the granitic gneiss and pegmatite plot in the A-type and S- and I-type granite field [55] (Figure 11A). Since the samples are characterized by low Fe-number, peraluminous rather than peralkaline, which together with the absence of sodic Mafic minerals, suggest that the A-type granite can be excluded [48]. Therefore, a convergent Margin setting is required for the parent Magma to receive both igneous and sedimentary sources. In the Nb-Y and Rb-Y + Nb diagrams, the granitic gneiss and pegmatite plot in the syn-collision granite and within plate granite fields, which, together with their peraluminous and alkali-calcic and alkalic signature, suggest a continental arc setting and the Magma was emplaced during the syn-collisional event [44] (Figure 11B,C). Low Sr/Y ratios and increasing Y contents also corroborate an arc affinity, indicating that the parent Magma was generated from an arc setting or partial melting of a rock that was formed within an arc [56] (Figure 11D). In the R1-R2 diagram, the rocks plot in the late orogenic to syn-collisional fields [57] (Figure 11E). Thus, the parent Magma of the AMC is generated in an arc setting near the collisional belt and the rocks formed via fractional crystallization and partial melting process during a syn-collisional event.

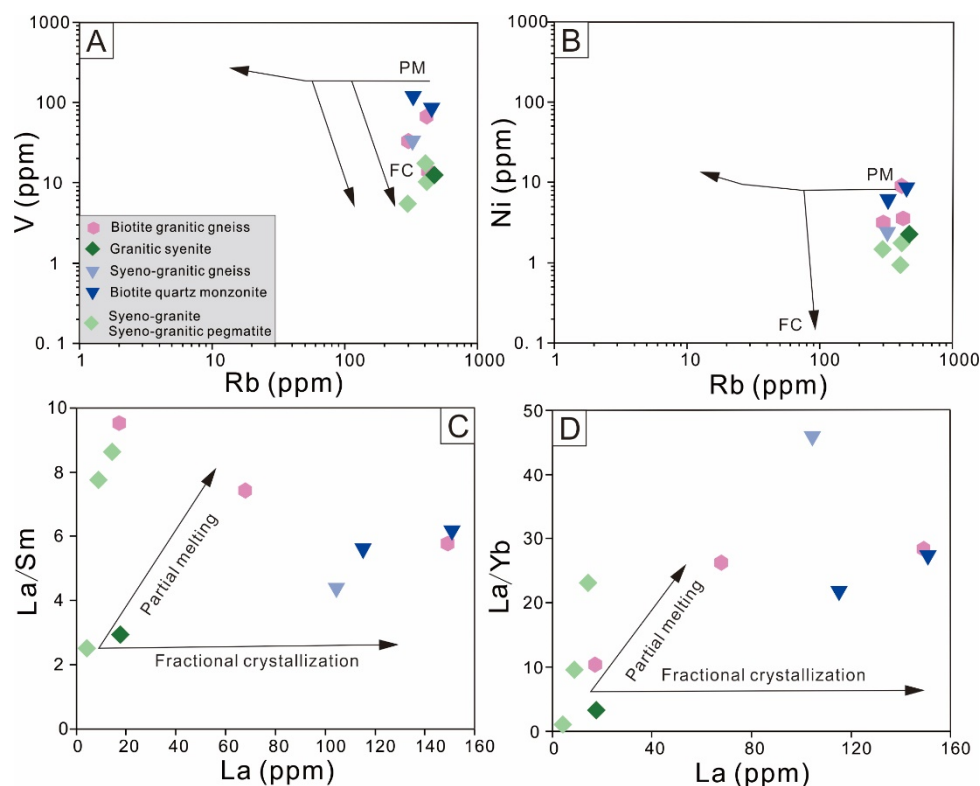


Figure 10. Compositional variation diagrams of (A,B) Ni, V vs. Rb diagrams of AMC basement rocks showing fractional crystallization After [53]. (C) La versus La/Sm and (D) La versus (La/Yb)_N for the AMC basement rocks showing partial melting and fractional crystallization, after [54].

5.2. Arc Building and Crust Evolution

The Proterozoic pre-Damara basement is broadly exposed in the Damara Orogenic Belt, surrounding cratonic Margins and orogenic belts of southern Africa, and these complexes were formed during the Paleoproterozoic Eburnian orogenic event [6,19]. The quartz-feldspathic orthogneiss of the pre-Damara basement from the south-western extension of the Abbabis Inlier near Rössing Uranium Mine of the Central Damara Belt show strong migmatization and are associated with Magma crystallization at 1196–1040 Ma, and minor xenocrytic zircons (2093–2014 Ma) are sourced from the Abbabis basement [21]. Longridge et al. [4] reported zircon U-Pb ages of 2026 Ma from the amphibolite of the Abbabis basement and correlate the complex with the Congo Craton. However, the basement gneiss and granitoids of the Epupa and Huab Complex of the pre-Damara basement from northern Namibia and Angola show Paleoproterozoic ages of 1810–1750 Ma and Neoproterozoic ages of 840–800 Ma, and are considered as part of the Congo Craton [1]. Negative ϵ_{Nd} values of 0 to -17 and high $\delta^{18}\text{O}$ values of +7.1 to +15.2‰ for the Neoproterozoic (750–450 Ma) granitic rocks from the center of the Damara Belt suggest partial melting of pre-existing basement [52].

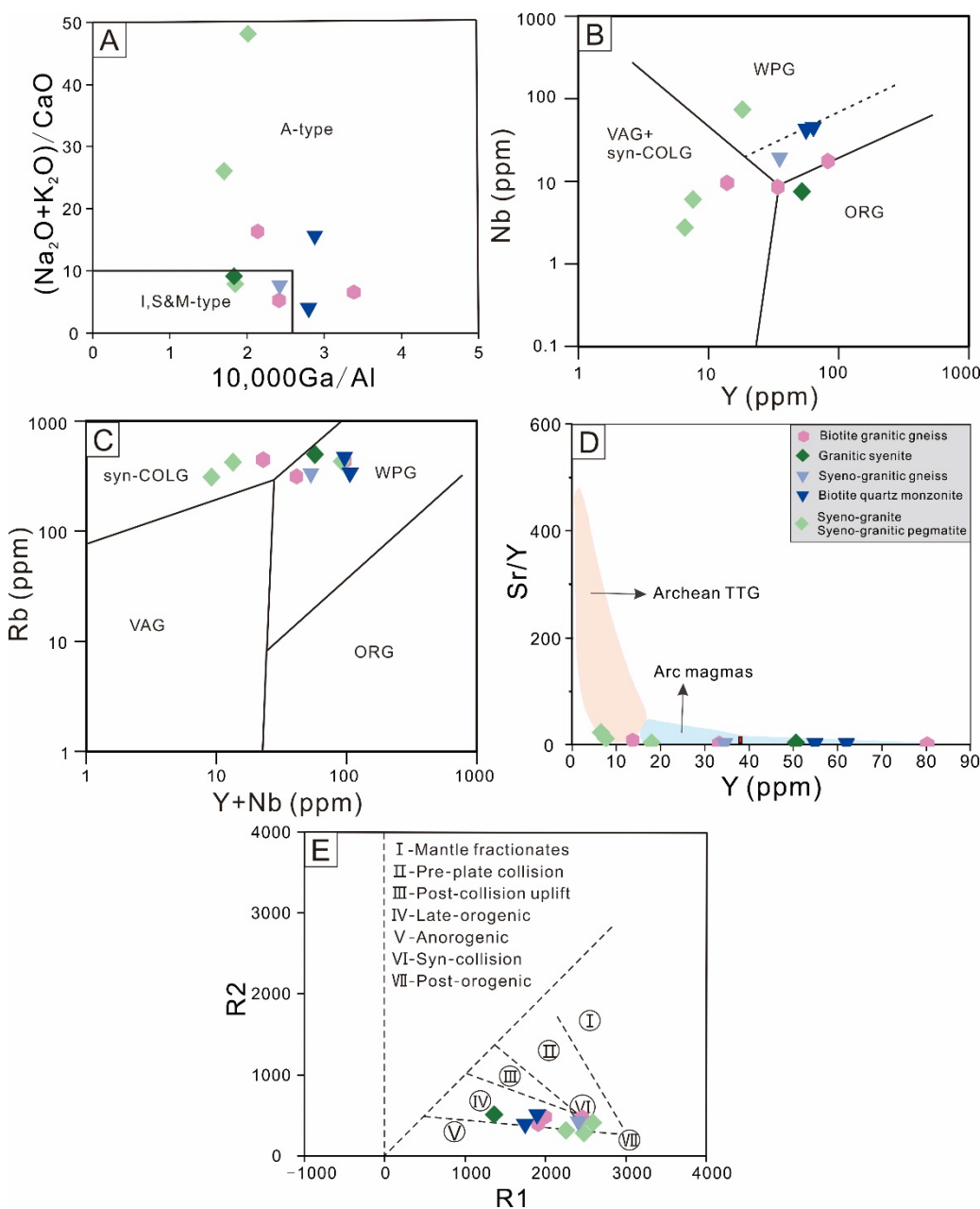


Figure 11. Petrogenetic discrimination diagrams (A) $(\text{Na}_2\text{O} + \text{K}_2\text{O})/\text{CaO}$ - $10,000\text{Ga}/\text{Al}$ [55]; (B) Nb-Y and (C) Rb-Y + Nb [44], (D) Sr/Y-Y [56], (E) R1-R2 cationic plot [57]. Abbreviations: VAG: Volcanic-arc granites, syn-COLG: Syn-collisional granites, WPG: Within plate granites, ORG: Ocean-ridge granites.

To the northeast, SHRIMP zircon U-Pb ages from the granitoid gneisses of the Tsodilo Hills Group of the Damara Belt in western Botswana also record Paleoproterozoic Magmatic ages of 2036–1978 Ma, which formed during the Eburnian orogenic event [58]. Further northeast, the migmatitic granite from the Magondi Orogenic Belt of northeast Botswana show Magmatic zircon U-Pb age of 2039 Ma and is correlated with the Paleoproterozoic orogeny between Kubu Island in the west of Sua Pan and the northwest of the Zimbabwe Craton [59]. Northeast to the Central African Copperbelt, the Katanga Supergroup comprises of 2.07–1.87 Ga Lufubu schist, granitoids and granitoid gneiss, and 1.06 Ga aplite and are considered as part of the extensive Paleoproterozoic arc equivalent to northern Namibia [60]. To the east of the Damara Orogenic Belt, the felsic gneiss from the Hohewarte Metamorphic Complex record Magmatic ages of 1758 Ma, 1290 Ma, and 1168 Ma, and are well correlated with the Abbas Complex and considered as part of the pre-Damara

basement accreted onto the Kalahari Craton [3]. The positive $\epsilon_{\text{Hf}}(t)$ values of +1.7 to +3.0 for the Paleoproterozoic (1758 Ma) quartzo-feldspathic gneiss, and +0.7 to +3.2 for the Mesoproterozoic gneiss (1290 Ma and 1168 Ma), suggest that the Magma sources for the Hohewarte Metamorphic Complex are derived from depleted Mantle [3].

To the northwest, in the Angolan Shield of SW Angola, the granite and ignimbrite also record Paleoproterozoic ages of 2.04–1.80 Ga, which formed in a Magmatic arc stretching from NW Zambia to NE Angola and Namibia [61]. In the nearby large exposure of the Epupa Metamorphic Complex of the southwestern Congo Craton, the amphibolite and orthogneiss show zircon U-Pb ages of 2027 Ma and 1862–1758 Ma and are correlated with the arc Magmatism of the Eburnian Orogenic event [4,6,19]. The gabbros sporadically exposed with the amphibolite and orthogneiss suggest that the Epupa Metamorphic Complex was generated in an arc setting [19]. The anatexis and migmatitic gneiss from the Epupa Metamorphic Complex show zircon U-Pb ages of 1762–1757 Ma and suggest prograde metamorphism and partial melting [6]. The augen gneiss, monzogranite and microgranite from the Okwa Basement Complex on the northwestern edge of the Kaapvaal craton show Paleoproterozoic ages of 2.10–2.06 Ga and might represent the eastern continuous Magmatic branch of the Paleoproterozoic basement [62]. Further south in the Namaqua-Natal Metamorphic Province, the granitoid orthogneisses also show crystallization ages of 1825–1810 Ma and variable $\epsilon_{\text{Hf}}(t)$ values of −24.34 to +3.03 with T_{DM} model ages of 2.41–1.67 Ga, suggesting the Magmas are dominantly derived from the Paleoproterozoic crust Material [60]. Geochemically, these granitoids are peraluminous to metaluminous and high-K alkaline and are equivalent to I-type granites formed in a Magmatic arc setting [63]. Thus, the extensive Paleoproterozoic Magmatic rocks and complexes in the Damara Orogenic belt and surrounding areas suggest multiple arc construction and May represent microcontinent fragments formed during the Eburnian orogenic event.

5.3. Metamorphism during the Damara Orogeny

In a recent study, Goscombe et al. [31] evaluated the metamorphic evolution history of the Damara Orogenic Belt and proposed that the Khomas Oceanic crust subduction initiates before 555 Ma, ocean closure and collision of the Congo and Kalahari cratons occurred at 555–550 Ma, peak metamorphism at 530–515 Ma, shortening associated with local extension at 515–505 Ma, and extension and exhumation at 505–470 Ma. Clemens and Kisters [64] reported gabbros, diorites, and granites from the Goas Intrusive Suite of the Southern Central Zone show bimodal composition and proposed that these rocks are formed through partial melting of the ancient crust at different depth levels during the subduction of the Khomas Oceanic Crust at ca. 580–575 Ma. Milani et al. [65] proposed that the 575 Ma Mafic to felsic rocks of the Goas Complex recorded the earliest Magmatism, and the variable $\epsilon_{\text{Hf}}(t)$ of −3.8 to −34.4 indicate that the Magma was dominantly sourced from the central-western African Paleoproterozoic Eburnean Orogen. Jung et al. [66,67] reported diorites, granodiorites and granites from the Oamikaub diorite (Goas Intrusive Suite) and Otjimbingswe alkaline complex of the northern Margin of the Southern Zone, which show variable initial ϵ_{Nd} values of −2.1 to −18.8 and suggest that ancient crust was involved in the Magma through a flat subduction process of the Kalahari Oceanic Crust and emplaced during the syn-collisional event of the Damara Orogeny at 545–563 Ma. However, Pontow et al. [68] reported a ca. 560 Ma from the Okamutambo alkaline Complex and variable initial ϵ_{Nd} values of −3.5 to −7.1, suggesting that the Magma May have been sourced from the Proterozoic crust within an extensional setting. The late Neoproterozoic (556–547 Ma) granodiorites, leucogranite and granites in the central Damara Orogenic Belt display variable $\epsilon_{\text{Nd}}(\text{init.})$ values of −7.2 to −20.6 and T_{DM} ages of 2.5–1.9 Ga, indicating they were formed by partial melting of the ca. 1.95 Ga Paleoproterozoic felsic basement [9,69,70]. The lithological sequence of the lower unit of diatexites, and granite plutons, middle unit of metataxesites, metasedimentary-sourced granitic rocks, and upper unit of metamorphic rocks with intrusive leucogranitic rocks from the Central Zone of the Damara orogenic belt represent an increasing degree of fractional crystallization and partial melting [33].

Longridge et al. [71] reported zircon and monazite ages of 520–510 Ma in the anatetic leucogranite from the southern Central Zone and correlate it with the extension and crust thinning process, and the 550–530 Ma Salem-type granite and Goes Suite are corresponding to the convergent shorting and crust thickening. Goscombe et al. [72] further divided the ca. 530–505 Ma Damara Orogenic event into peak metamorphism and NW-SE to NNW-SSE shortening at ca. 530–525 Ma, E-W shorting at ca. 508 Ma, and N-S extension and thinning of the orogenic core at ca. 505 Ma. In terms of the peak metamorphic P - T condition, the Central Zone experienced lower metamorphic conditions than the North and South Zone, being 637 °C and 10.4 kbar for the east Northern Zone, 760–800 °C and 4.4–6.2 kbar for the Central Zone, 550–640 °C and 8.6–11.2 kbar for the Southern Zone [31]. High temperatures and low pressures in the Central Zone indicate crustal melting during uplift and thickening corresponding to an extensional process during the collision of the Congo and Kalahari Cratons at 505–407 Ma [31,48,73].

Therefore, the metamorphic data from the biotite granitic gneisses, syeno-granite, and syeno-granitic pegmatites of this study suggest the Abbabis basement rocks May have undergone low pressure and high temperature partial melting and metamorphism during the Damara Orogenic event. The 581–535 Ma ages are consistent with the Khomas oceanic crust subduction and early collision of the Kalahari and Congo Cratons, 531–522 Ma corresponds to the syn-collisional peak metamorphism, and 518–484 Ma corresponds to the post-collision [31,60–68]. In addition to metamorphism, extensive intermediate to felsic Magmatic rocks within the Damara Orogenic Belt were generated during syn-collisional and post-collisional metamorphism [66,67,73]. Simon et al. [9] reported an age of 547 Ma from the calcic to calc-alkalic diorite and leucogranite of the Achas intrusion and suggested the intermediate igneous rocks were formed by partial melting of the Proterozoic basement during the synorogenic process of the Damara Orogeny. Jung et al. [50] reported negative $\varepsilon_{\text{Nd}}^{\text{t}}$ values of –4.1 to –10 and T_{DM} age of 2.5–1.9 Ga from the peraluminous and alkalic and calc-alkalic 530 Ma pegmatite and aplite of the Donkerhoek batholith and suggest the Magma was sourced from the meta-igneous basement and emplaced during the syn-tectonic Damara Orogeny. Fan et al., [8] reported negative $\varepsilon_{\text{Nd}}^{\text{t}}$ values of –14.8 to –16.5 and T_{DM}^2 of 2.56–2.43 Ga from the 506–497 Ma uraniferous leucogranite from the uranium deposit area in the Gaudeanmus and suggest the Main source for uranium primary mineralization was derived from the Paleoproterozoic basement. Cross et al. [74] reported U-Th-Pb age of 496 Ma from the uraninite of a leucogranite in the Husab uranium deposit and suggested that the age represents uranium mineralization. Briqueu et al. [75] and Cuney and Kuser [76] interpreted the monazite and uraninite ages of 508–509 Ma from the leucogranite of the Goanikonte as the uranium mineralization age, and the Magma was emplaced during metamorphism and partial melting of Damara Orogenic Event. Therefore, the metamorphic ages from the Abbabis Metamorphic Complex are consistent with the mineralization ages from uranium deposit, which, together with the negative $\varepsilon_{\text{Nd}}^{\text{t}}$ values and the Paleoproterozoic model ages of the Cambrian leucogranite, indicating that the Magma provenance for the intrusive rocks and uranium might source from the Paleoproterozoic basement.

6. Conclusions

The following general conclusions can be drawn from the present study:

1. The biotite granitic gneiss, syeno-granite, syeno-granitic pegmatite, syeno-granitic gneiss, granitic syenite, and biotite quartz monzonite are highly evolved and formed by a fractional crystallization process during the Paleoproterozoic, and experienced variable degrees of partial melting during the late Proterozoic Damara Orogenic event.
2. A review of the Paleoproterozoic basement rocks show that the Paleoproterozoic AMC basement rock was correlated well with the extensive Paleoproterozoic Magmatic complexes in southern Africa, which were formed during the Paleoproterozoic Eburnian orogenic event.

3. Late Paleozoic to Cambrian Magmatic rocks and the primary uranium mineralization source in the Damara Orogenic belt are formed by partial melting of the AMC basement during the subduction-collision-extension process of the Damara Orogenic event.

Author Contributions: Conceptualization: K.-F.Q.; writing: S.-S.L.; review and editing: W.Z. and H.-F.Z.; formal analysis: L.W. and E.T.S. All authors have read and agreed to the published version of the Manuscript.

Funding: This research was funded by the National Natural Science Foundation of China (42111530124), Beijing Nova Program (Z201100006820097), 111 Project of the Ministry of Science and Technology (BP0719021), China Geological Survey, uranium resources survey in Namibia and Botswana (DD20201148), Chinese Postdoctoral Science Foundation (2021M692995), and mLR Key Laboratory of Metallogeny and Mineral Assessment, Institute of Mineral Resources, Chinese Academy of Geological Sciences (ZS2003).

Data Availability Statement: Not applicable.

Acknowledgments: We thank H.G. Dill and two three anonymous referees for their constructive and insightful comments which greatly improved this Manuscript. The authors thank Zeyu Yang, Yizhan Sun, Zechen Xi, and Yixue Gao for their help in figure preparation.

Conflicts of Interest: The authors declare no conflict of interest.

References

1. Tegtmeier, A.; Kröner, A. U-Pb zircon ages for granitoid gneisses in northern Namibia and their significance for Proterozoic crustal evolution of southwestern Africa. *Precambrian Res.* **1985**, *28*, 311–326. [[CrossRef](#)]
2. Miller, R.M. *Volume 2: Neoproterozoic to Lower Palaeozoic*; Geological Survey of Namibia: Windhoek, Namibia, 2008.
3. Mapani, B.; Cornell, D.; van Schijndel, V. Geochronology and tectonic evolution of the hohewarte complex, central namibia: New insights into paleoproterozoic to early neoproterozoic crustal accretion processes. *J. Afr. Earth Sci.* **2014**, *99*, 228–244. [[CrossRef](#)]
4. Longridge, L.; Kinnaird, J.A.; Gibson, R.L.; Armstrong, R.A. Amphibolites of the central zone: New SHRIMP U-Pb ages and implications for the evolution of the Damara Orogen, Namibia. *S. Afr. J. Geol.* **2014**, *117*, 67–86. [[CrossRef](#)]
5. Goscombe, B.; Foster, D.A.; Gray, D.; Wade, B. Assembly of central Gondwana along the Zambezi Belt: Metamorphic response and basement reactivation during the Kuunga Orogeny. *Gondwana Res.* **2020**, *80*, 410–465. [[CrossRef](#)]
6. Kröner, A.; Rojas-Agramonte, Y.; Hegner, E.; Hoffmann, K.-H.; Wingate, M.T.D. SHRIMP zircon dating and Nd isotopic systematics of Palaeoproterozoic migmatitic orthogneisses in the Epupa Metamorphic Complex of northwestern Namibia. *Precambr. Res.* **2010**, *183*, 50–69. [[CrossRef](#)]
7. Goscombe, B.; Hand, M.; Gray, D.; Mawby, J. The metamorphic architecture of a transpressional orogeny: The Kaoko Belt, Namibia. *J. Petrol.* **2003**, *44*, 679–711. [[CrossRef](#)]
8. Fan, H.; Chen, J.; Wang, S.; Zhao, J.; Dazhao, G.U.; Meng, Y. Genesis and uranium sources of leucogranite-hosted uranium deposits in the gaudeanmus area, central damara belt, namibia: Study of element and nd isotope geochemistry. *Acta Geol. Sin.* **2017**, *91*, 2126–2137. [[CrossRef](#)]
9. Simon, I.; Jung, S.; Romer, R.L.; Garbe-Schönberg, D.; Berndt, J. Geochemical and Nd-Sr-Pb isotope characteristics of synorogenic lower crust-derived granodiorites (Central Damara orogen, Namibia). *Lithos* **2017**, *274–275*, 397–411. [[CrossRef](#)]
10. Qiu, K.F.; Yu, H.C.; Wu, M.Q.; Geng, J.Z.; Taylor, R.D. Discrete Zr and REE mineralization of the Baerzhe rare-metal deposit, China. *Am. Mineral.* **2019**, *104*, 1487–1502. [[CrossRef](#)]
11. Dill, H.G. Pegmatites and aplites: Their genetic and applied ore geology. *Ore Geol. Rev.* **2015**, *69*, 417–561. [[CrossRef](#)]
12. Dahlkamp, F.J. *Uranium Deposits of the World*; Springer: Berlin/Heidelberg, Germany, 2016.
13. Ashworth, L.; Kinnaird, J.A.; Nex, P.; Harris, C.; Müller, A.B. Origin of rare-element-mineralized damara belt pegmatites: A geochemical and light stable isotope study. *Lithos* **2020**, *372–373*, 105655. [[CrossRef](#)]
14. Chen, J.Y.; Fan, H.H.; Wang, Y.S.; Gu, D.Z.; Zhang, C.; Chen, D.H. The sulfide characteristics and S-Pb isotopic composition of leucogranite-type uranium deposit in the Gaudeanmus area, central Damara belt, Namibia. *Acta Geol. Sin.* **2020**, *94*, 587–598.
15. Han, J.; Chen, J.Y.; Fan, H.H.; Wang, S.Y.; Chen, D.H.; Xiu, Q.Y. Research on metallogenesis of the alaskite-type uranium deposits in the Rossing area, Namibia. *Acta Geol. Sin.* **2021**, *95*, 1019–1028.
16. Gray, T.; Kinnaird, J.; Laberge, J.; Caballero, A. Uraniferous Leucogranites in the Rössing Area, Namibia: New Insights from Geologic Mapping and Airborne Hyperspectral Imagery. *Econ. Geol.* **2021**, *116*, 1409–1434. [[CrossRef](#)]
17. Huang, R.X.; Wang, G.S.; Yuan, G.L.; Qiu, K.F.; Hounkpe, J.B. Assimilation and fractional crystallization (AFC) process of pegmatitic Magma and its implications for uranium mineralization:A case study of the Husab uranium deposit, Namibia. *Earth Sci. Front.* **2020**, *1*, 1–33.
18. Qiu, K.F.; Goldfarb, R.J.; Deng, J.; Yu, H.C.; Gou, Z.Y.; Ding, C.J.; Wang, Z.K.; Li, D.P. Gold deposits of the Jiaodong Peninsula, eastern China. *Soc. Econ. Geol. Spec. Publ.* **2020**, *23*, 753–773.

19. Kröner, A.; Rojas-Agramonte, Y.; Wong, J.; Wilde, S.A. Zircon reconnaissance dating of Proterozoic gneisses along the Kunene River of northwestern Namibia. *Tectonophysics* **2015**, *662*, 125–139. [[CrossRef](#)]
20. Li, S.S.; Palin, R.M.; Santosh, M.; Shaji, E.; Tsunogae, T. Extreme thermal metamorphism associated with Gondwana assembly: Evidence from sapphirine-bearing granulites of Rajapalayam, southern India. *Geol. Soc. Am. Bull.* **2020**, *132*, 1013–1030. [[CrossRef](#)]
21. Kröner, A.; Retief, E.A.; Compston, W.; Jacob, E.R.; Burger, A.J. Single-age and conventional zircon dating of remobilised basement gneisses in the central Damara belt of Namibia. *S. Afr. J. Geol.* **1991**, *94*, 379–387.
22. Gray, D.R.; Foster, D.A.; Meert, J.G.; Goscombe, B.D.; Armstrong, R.; Trouw, R.A.J.; Passchier, C.W. A Damara orogen perspective on the assembly of southwestern Gondwana. In *West Gondwana: Pre-Cenozoic Correlations Across the South Atlantic Region*; Pankhurst, R.J., Trouw, R.A.J., Brito Neves, B.B., De Wit, M.J., Eds.; Geological Society of London Special Publication: London, UK, 2008; Volume 294, pp. 257–278.
23. John, T.; Schenk, V.; Mezger, K.; Tembo, F. Timing and PT evolution of whiteschist metamorphism in the Lufilian arc-Zambezi belt orogen (Zambia): Implications for the assembly of Gondwana. *J. Geol.* **2004**, *112*, 71–90. [[CrossRef](#)]
24. Jung, S.; Mezger, K.; Hoernes, S. Petrology of basement-dominated terranes. II: Contrasting isotopic (Sr, Nd, Pb, O) signatures of basement-derived granites and constraints on the source region of granite (Damara orogen, Namibia). *Chem. Geol.* **2003**, *199*, 1–28. [[CrossRef](#)]
25. Meneghini, F.; Kisters, A.; Buick, I.; Fagereng, Å. Fingerprints of late Neoproterozoic ridge subduction in the Pan-African Damara belt, Namibia. *Geology* **2014**, *42*, 903–906. [[CrossRef](#)]
26. Qiu, K.F.; Yu, H.C.; Deng, J.; McIntire, D.; Gou, Z.Y.; Geng, J.Z.; Chang, Z.S.; Zhu, R.; Li, K.N.; Goldfarb, R. The giant Zaozigou Au-Sb deposit in West Qinling, China: Magmatic- or metamorphic-hydrothermal origin? *Miner. Depos.* **2020**, *18*, 345–362. [[CrossRef](#)]
27. Henry, G.; Clendenin, C.W.; Stanistreet, I.G.; Maiden, K.J. Multiple detachment model for the early rifting stage of the Late Proterozoic Damara orogen in Namibia. *Geology* **1990**, *18*, 67–71. [[CrossRef](#)]
28. Nascimento, D.B.; Schmitt, R.S.; Ribeiro, A.; Trouw, R.A.J.; Passchier, C.W.; Baser, M.A.S. Depositional ages and provenance of the Neoproterozoic Damara Supergroup (northwest Namibia): Implications for the Angola-Congo and Kalahari cratons connection. *Gondwana Res.* **2017**, *52*, 153–171. [[CrossRef](#)]
29. Foster, D.A.; Goscombe, B.D.; Newstead, B.; Mapani, B.; Mueller, P.A.; Gregory, L.C.; Muvanga, E. U-Pb age and Lu-Hf isotopic data of detrital zircons from Neoproterozoic Damara Sequence: Implications for pre-Gondwana proximity of Congo and Kalahari. *Gondwana Res.* **2015**, *28*, 179–190. [[CrossRef](#)]
30. Kitt, S.; Kisters, A.; Steven, N.; Maiden, K.; Hartmann, K. Shear-zone hosted copper mineralisation of the Omitiomire deposit—structural controls of fluid flow and mineralisation during subduction accretion in the Pan-African Damara Belt of Namibia. *Ore Geol. Rev.* **2016**, *75*, 1–15. [[CrossRef](#)]
31. Goscombe, B.; Foster, D.; Gray, D.; Wade, B. Metamorphic response and crustal architecture in a classic collisional orogen: Damara Belt, Namibia. *Gondwana Res. Focus Rev.* **2017**, *52*, 80–124. [[CrossRef](#)]
32. Longridge, L.; Gibson, R.L.; Kinnaird, J.A.; Armstrong, R.A. Constraining the timing of deformation in the southwestern Central Zone of the Damara Belt, Namibia. *Geol. Soc. Lond. Spec. Publ.* **2011**, *357*, 107–135. [[CrossRef](#)]
33. Toé, W.; Vanderhaeghe, O.; Andre-Mayer, A.S.; Feybesse, J.L.; Milesi, J.P. From migmatites to granites in the Pan-African Damara orogenic belt, Namibia. *J. Afr. Earth Sci.* **2013**, *85*, 62–74. [[CrossRef](#)]
34. Kisters, A.F.M.; Jordaan, L.S.; Neumaier, K. Thrust-related dome structures in the Karibib district and the origin of orthogonal fabric domains in the South Central Zone of the Pan-African Damara belt, Namibia. *Precambr. Res.* **2004**, *133*, 283–303. [[CrossRef](#)]
35. Hall, D.; Kisters, A. From steep feeders to tabular plutons—Emplacement controls of syntectonic granitoid plutons in the Damara belt, Namibia. *J. Afr. Earth Sci.* **2016**, *113*, 51–64. [[CrossRef](#)]
36. Li, C.; Wang, D.H.; Qu, W.J.; Meng, H.M.; Zhou, L.M.; Fan, X.T.; Li, X.W.; Zhao, H.; Wen, H.L.; Sun, P.C. A Review and Perspective on Analytical Methods of Critical Metal Elements. *Rock Miner. Anal.* **2020**, *39*, 658–669.
37. Hu, Z.C.; Zhang, W.; Liu, Y.S.; Gao, S.; Li, M.; Zong, K.Q.; Chen, H.H.; Hu, S.H. “Wave” signal smoothing and mercury removing device for laser ablation quadrupole and multiple collector ICP-MS analysis: Application to lead isotope analysis. *Anal. Chem.* **2015**, *87*, 1152–1157. [[CrossRef](#)]
38. Zong, K.Q.; Chen, J.Y.; Hu, Z.C.; Liu, Y.S.; Li, M.; Fan, H.H.; Meng, Y.N. In-situ U-Pb dating of uraninite by fs-LA-ICP-MS. *Sci. China Earth Sci.* **2015**, *58*, 1731–1740. [[CrossRef](#)]
39. Liu, Y.S.; Hu, Z.C.; Gao, S.; Günther, D.; Xu, J.; Gao, C.G.; Chen, H.H. In situ analysis of Major and trace elements of anhydrous minerals by LA-ICP-MS without applying an internal standard. *Chem. Geol.* **2008**, *257*, 34–43. [[CrossRef](#)]
40. Liu, Y.S.; Gao, S.; Hu, Z.C.; Gao, C.G.; Zong, K.Q.; Wang, D.B. Continental and oceanic crust recycling-induced melt-peridotite interactions in the Trans-North China Orogen: U-Pb dating, Hf isotopes and trace elements in zircons of Mantle xenoliths. *J. Petrol.* **2010**, *51*, 537–571. [[CrossRef](#)]
41. Ludwig, K.R. *ISOPLOT 3.00: A Geochronological Toolkit for Microsoft Excel*; Berkeley Geochronology Center: Berkeley, CA, USA, 2003; p. 39.
42. Sawyer, E.W. Migmatites formed by water-fluxed partial melting of a leucogranodiorite protolith: Microstructures in the residual rocks and source of the fluid. *Lithos* **2010**, *116*, 273–286. [[CrossRef](#)]
43. He, Q.; Zhang, S.B.; Zheng, Y.F.; Chen, R.X. Peritectic minerals record partial melting of the deeply subducted continental crust in the Sulu orogen. *J. Metam. Geol.* **2022**, *40*, 87–120. [[CrossRef](#)]

44. Middlemost, E.A.K. Naming Materials in the Magma/igneous rock system. *Earth Sci. Rev.* **1994**, *37*, 215–224. [[CrossRef](#)]
45. Frost, B.R.; Barnes, C.G.; Collins, W.J.; Arculus, R.J.; Ellis, D.J.; Frost, C.D. A geochemical classification for granitic rocks. *J. Petrol.* **2001**, *42*, 2033–2048. [[CrossRef](#)]
46. Maniar, P.D.; Piccoli, P.M. Tectonic discrimination of granitoids. *Geol. Soc. Am. Bull.* **1989**, *101*, 635–643. [[CrossRef](#)]
47. Sun, S.-S.; McDonough, W.F. Chemical and isotopic systematics of oceanic basalts: Implications for Mantle composition and processes. In *Magmatism in the Ocean Basins*. Geological Society London Special Publications; Saunders, A.D., Norry, M.J., Eds.; Geological Society of London: London, UK, 1989; Volume 42, pp. 313–345.
48. Pearce, J.A.; Harris, N.B.W.; Tindle, A.G. Trace element discrimination diagrams for the tectonic interpretation of granitic rocks. *J. Petrol.* **1984**, *25*, 956–983. [[CrossRef](#)]
49. Patiño Douce, A.E. What do experiments tell us about the relative contributions of crust and Mantle to the origin of granitic Magmas. *Geol. Soc. Lond. Spec. Publ.* **1999**, *168*, 55–75. [[CrossRef](#)]
50. White, J.C.; Parker, D.F.; Ren, M. The origin of trachyte and pantellerite from Pantelleria, Italy: Insights from Major element, trace element and thermodynamic modelling. *J. Volcanol. Geotherm. Res.* **2009**, *179*, 33–55. [[CrossRef](#)]
51. Jung, S.; Hauff, F. Petrogenesis of a low- $^{87}\text{Sr}/^{86}\text{Sr}$, two-mica, garnet-bearing leucogranite (Donkerhoek batholith, Damara orogen, Namibia). *J. Afr. Earth Sci.* **2021**, *174*, 104055. [[CrossRef](#)]
52. Hawkesworth, C.J.; Menzies, M.A.; van Calsteren, P. Geochemical and tectonic evolution of the Damara Belt, Namibia. *Collis. Tecton. Geol. Soc. Spec. Publ.* **1986**, *19*, 305–319. [[CrossRef](#)]
53. Schiano, P.; Monzier, M.; Eissen, J.P. Simple mixing as the Major control of the evolution of volcanic suites in the Ecuadorian Andes. *Contrib. Mineral. Petr.* **2010**, *160*, 297–312. [[CrossRef](#)]
54. De Souza, Z.S.; Martin, H.; Peucat, J.J.; Jardim de Sá, E.F.; de Freitas Macedo, M.H. Calc-Alkaline Magmatism at the Archean-Proterozoic Transition: The Caicoó Complex Basement (NE Brazil). *J. Petrol.* **2007**, *48*, 2149–2185. [[CrossRef](#)]
55. Whalen, B.J.; Currie, K.L.; Chappell, B.W. A-type granites: Geochemical characteristics, discrimination and petrogenesis. *Contrib. Mineral. Petr.* **1987**, *95*, 407–419. [[CrossRef](#)]
56. Defant, M.J.; Drummond, M.S. Derivation of some modern arc Magmas by melting of young subducted lithosphere. *Nature* **1990**, *367*, 662–665. [[CrossRef](#)]
57. Batchelor, R.A.; Bowden, P. Petrogenetic interpretation of granitic rock series using multicationic parameters. *Chem. Geol.* **1985**, *48*, 43–55. [[CrossRef](#)]
58. Mapeo, R.; Wendorff, M.; Ramokate, L.V.; Armstrong, R.A.; Mphinyane, T.; Koobokile, M. Zircon geochronology of basement granitoid gneisses and sedimentary rocks of the Tsodilo Hills Group in the Pan-African Damara Belt, western Botswana: Age constraints, provenance, and tectonic significance. *J. Afr. Earth Sci.* **2019**, *159*, 103576. [[CrossRef](#)]
59. Majaula, T.; Hanson, R.E.; Key, R.M.; Singletary, S.J.; Martin, W.W.; Bowring, S.A. The Magondi Belt in northeast Botswana: Regional relations and new geochronological data from the Sua Pan area. *J. Afr. Earth Sci.* **2001**, *32*, 257–267. [[CrossRef](#)]
60. Rainaud, C.; Master, S.; Armstrong, R.A.; Robb, L.J. Geochronology and nature of the paleoproterozoic basement in the central african copper belt (Zambia and democratic republic of Congo), with regional implications. *J. Afr. Earth Sci.* **2005**, *42*, 1–31. [[CrossRef](#)]
61. McCourt, S.; Armstrong, R.A.; Jelsma, H.; Mapeo, R.B.M. New U-Pb SHRIMP ages from Lubango region, SW Angola: Insights into the palaeoproterozoic evolution of the Angolan Shield, southern Congo craton, Africa. *J. Geological. Soc. Lond.* **2013**, *170*, 353–363. [[CrossRef](#)]
62. Mapeo, R.B.M.; Ramokate, L.V.; Corfu, F.; Davis, D.W.; Kampunzu, A.B. The Okwa basement complex, western Botswana: U-Pb zircon geochronology and implications for eburnean processes in southern Africa. *J. Afr. Earth Sci.* **2006**, *46*, 253–262. [[CrossRef](#)]
63. Nke, A.Y.; Bailie, R.H.; Macey, P.H.; Thomas, R.J.; Frei, D.; Roux, P.L.; Spencer, C.J. The 1.8 Ga Gladkop suite: The youngest Palaeoproterozoic domain in the Namaqua-Natal Metamorphic Province, South Africa. *Precambrian Res.* **2020**, *350*, 105941. [[CrossRef](#)]
64. Clemens, J.D.; Kisters, A.F.M. Magmatic indicators of subduction initiation: The bimodal Goas intrusive Suite in the Pan-African Damara Belt of Namibia. *Precambrian Res.* **2021**, *362*, 106309. [[CrossRef](#)]
65. Milani, L.; Kinnaird, J.A.; Lehmann, J.; Naydenov, K.V.; Saalmann, K.; Frei, D.; Gerdes, A. Role of crustal contribution in the early stage of the Damara Orogen, Namibia: New constraints from combined U-Pb and Lu-Hf isotopes from the Goas Magmatic Complex. *Gondwana Res.* **2015**, *28*, 961–986. [[CrossRef](#)]
66. Jung, S.; Hauff, F.; Berndt, J. Generation of a potassic to ultrapotassic alkaline complex in a syncollisional setting through flat subduction: Constraints on Magma sources and processes (Otjimbingswe alkaline complex, Damara orogen, Namibia). *Gondwana Res.* **2020**, *82*, 267–287. [[CrossRef](#)]
67. Jung, S.; Pfander, J.A.; Hauff, F.; Berndt, J. Crust-mantle interaction during syn-collisional Magmatism—Evidence from the Oamikaub diorite and Neikhoes metagabbro (Damara orogen, Namibia). *Precambrian Res.* **2020**, *351*, 105955. [[CrossRef](#)]
68. Pontow, R.; Jung, S.; Hauff, F.; Berndt, J. Melting of metasomatically enriched lithospheric Mantle—Constraints from Pan-African monzonites (Damara Orogen, Namibia). *Lithos* **2021**, *398–399*, 106332. [[CrossRef](#)]
69. Yu, H.C.; Qiu, K.F.; Hetherington, C.J.; Chew, D.; Huang, Y.Q.; He, D.Y.; Geng, J.Z.; Xian, H.Y. Apatite as an alternative petrochronometer to trace the evolution of Magmatic systems containing metamict zircon. *Contrib. Mineral. Petr.* **2021**, *176*, 68. [[CrossRef](#)]

70. Stammerier, J.; Jung, S.; Romer, R.L.; Berndt, J.; Garbe-Schönberg, D. Petrology of ferroan alkali-calcic granites: Synorogenic high-temperature melting of undepleted felsic lower crust (Damara orogen, Namibia). *Lithos* **2015**, *224–225*, 114–125. [[CrossRef](#)]
71. Longridge, L.; Gibson, R.L.; Kinnaird, J.A.; Armstrong, R.A. New constraints on the age and conditions of LPHT metamorphism in the southwestern Central Zone of the Damara Belt, Namibia and implications for tectonic setting. *Lithos* **2017**, *278–281*, 361–382. [[CrossRef](#)]
72. Goscombe, B.; Foster, D.A.; Gray, D.; Wade, B.; Marsellos, A.; Titus, J. Deformation correlations, stress field switches and evolution of an orogenic intersection: The Pan African Kaoko-Damara orogenic junction, Namibia. *Geosci. Front.* **2017**, *8*, 1187–1232. [[CrossRef](#)]
73. Jung, S.; Brandt, S.; Bast, R.; Scherer, E.E.; Berndt, J. Metamorphic petrology of a high—T/low—P granulite terrane (Damara Belt, Namibia)—constraints from pseudosection modelling and high—precision Lu—Hf garnet-whole rock dating. *J. Metam. Geol.* **2019**, *37*, 41–69. [[CrossRef](#)]
74. Cross, A.; Jaireth, S.J.; Rapp, R.; Armstrong, R. Reconnaissance-style EPMA chemical U–Th–Pb dating of uraninite. *Aust. J. Earth Sci.* **2022**, *58*, 675–683. [[CrossRef](#)]
75. Briqueu, L.; Lancelot, J.; Valois, J.P.; Walgenwitz, F. Géochronologie U–Pb et genése d’un type de mineralisation uranifère: Les alaskites de Goanikontès (Namibie) et leur encaissant. *Bull. Des Cent. De Rech. Explor. Prod. Elf-Aquitaine* **1980**, *4*, 759–811.
76. Cuney, M.; Kyser, K. *Recent and Not-So-Recent Developments in Uranium Deposits and Implications for Exploration*; Mineralogical Association of Canada: Quebec City, QC, Canada, 2008.